Solution structure of deglycosylated human IgG1 shows the role of C_H2 glycans in its conformation

Valentina A. Spiteri[1], James Doutch[2], Robert P. Rambo[3], Jayesh Gor[1], Paul A. Dalby[4] and Stephen J. Perkins[1*]

From the [1]Department of Structural and Molecular Biology, Division of Biosciences, Darwin Building, University College London, Gower Street, London WC1E 6BT, U.K.;
[2] ISIS Facility, STFC Rutherford Appleton Laboratory, Harwell Campus, Didcot, Oxfordshire, OX11 0QX, UK;
[3] Diamond Light Source Ltd., Diamond House, Harwell Science and Innovation Campus, Chilton, Didcot, Oxfordshire, OX11 0DE, UK;
[4] Department of Biochemical Engineering, University College London, Gordon Street, London, WC1E 7JE, UK.

ORCID identifiers: Valentina A. Spiteri 0000-0002-5002-4989, Robert P. Rambo 0000-0003-2546-1615, Jayesh Gor 0000-0002-1654-1392, Paul A. Dalby 0000-0002-0980-8167, Stephen J. Perkins 0000-0001-9218-9805

Running Title: Deglycosylated IgG1 solution structure

* Author to whom correspondence and requests for reprints should be addressed (SJP: Tel: 020-7679-7048; Fax: 020-7679-7193; email s.perkins@ucl.ac.uk).

ABSTRACT
The human immunoglobulin G (IgG) class is the most prevalent antibody in serum, with the IgG1 subclass being the most abundant. IgG1 is comprised of two Fab regions connected to a Fc region through a 15-residue hinge peptide. Two glycan chains are conserved in the Fc region in IgG, however their importance for the structure of intact IgG1 has remained unclear. Here, we subjected glycosylated and deglycosylated monoclonal human IgG1 (designated as A33) to a comparative multidisciplinary structural study of both forms. Following deglycosylation using PNGase F, analytical ultracentrifugation showed that IgG1 remained monomeric and the sedimentation coefficients $s^0_{20,w}$ of IgG1 decreased from 6.45 S by 0.16-0.27 S. This change was attributed to the reduction in mass following glycan removal. X-ray and neutron scattering revealed changes in the Guinier structural parameters after deglycosylation. While the radius of gyration R_G was unchanged, the cross-sectional radius of gyration, $R_{XS\text{-}1}$, increased by 0.1 nm and the commonly occurring distance peak *M2* of the distance distribution curve *P(r)* increased by 0.4 nm. These changes revealed that the Fab-Fc separation in IgG1 was perturbed following deglycosylation. To explain these changes, atomistic scattering modelling based on Monte Carlo simulations resulted in 123,284 and 119,191 trial structures for glycosylated and deglycosylated IgG1 respectively. From these, 100 X-ray and neutron best-fit models were determined. For these, principal component analyses identified five groups of structural conformations that were different for glycosylated and deglycosylated IgG1. The Fc region in glycosylated IgG1 showed a restricted range of conformations relative to the Fab regions, while the Fc region in deglycosylated IgG1 showed a broader conformational spectrum. These more variable Fc conformations account for the loss of binding to the FcγR receptor in deglycosylated IgG1.

Keywords: Analytical ultracentrifugation; antibody modelling; small-angle neutron scattering; human IgG subclasses; small angle X-ray scattering.

Abbreviations: IgG1, immunoglobulin G subclass 1; MC, Monte Carlo; MD, molecular dynamics; PCA, principal component analyses; R_G, radius of gyration; SANS, small angle neutron scattering; SAXS, small angle X-ray scattering.

SIGNIFICANCE
Human IgG1 antibody possesses two conserved glycans in its Fc region with unknown structural significance. Here, we established the role of the glycans in the overall structure of human IgG1. First, analytical ultracentrifugation revealed monomeric structures after enzymatic glycan removal, showing these were unaffected. Next, X-ray and neutron scattering revealed observable conformational changes in IgG1 after glycan removal. Atomistic Monte Carlo modelling fits of the IgG1 scattering curves showed that the best-fit structures after deglycosylation were different from the glycosylated best-fit structures. The Fc region occupied more conformational space. This greater flexibility after deglycosylation reveals the importance of the glycans in stabilizing the Fc regions and affects the way in which the Fc region interacts with its Fc receptors.

INTRODUCTION
Immunoglobulins are an important class of humoral (adaptive) glycoproteins, composing of 82-96% protein and 4-18% carbohydrate (1). The most abundant immunoglobulin class in human serum is IgG, a Y-shaped molecule that is found as four subclasses, namely IgG1, IgG2, IgG3 and IgG4, which occur at 8.0 mg/ml, 4.0 mg/ml, 0.8 mg/ml and 0.4 mg/ml in serum (2). The structure of IgG1 is formed as two Fab regions, which bind with high specificity and affinity to a specific antigen, and an Fc region which binds to

Fcγ receptors (FcγRs) on the surface of immune cells, and to complement C1q to initiate the classical pathway of activation (Figure 1*A*). In IgG1, the Fabs and the Fc regions are connected by a 15- residue hinge held together by two disulphide bonds at Cys^{226} and Cys^{229} in the hinge (1). As well as being the most abundant class in serum, IgG1 is the predominant class used in therapeutic antibodies, where 54 IgG1 monoclonal antibodies are commercially available out of a total of 83 antibody-based products in a multibillion dollar industry (3).

The conserved N-linked glycosylation in the Fc region plays a key functional role in all four IgG subclasses (Figure 1*B*). A complex-type biantennary glycan with a $Man_3GlcNAc_2$ core and two NeuNAc.Gal.GlcNAc antennae is attached at Asn^{297} on each C_H2 domain (4) (Figure 2). However, the glycan structure is chemically heterogenous (5). The Fc glycans modulate several IgG-Fc effector functions (6). Glycoengineering is becoming increasingly important in order to elicit desired responses. For example, afucosylated IgG1 is able to activate a natural killer antibody-dependent cellular cytotoxicity response more effectively for reason of its increased affinity for FcγRIIIa (7,8). Deglycosylated antibodies may be good candidates for therapeutics if a lower propensity to activate inflammatory cascades is desirable, because the removal of glycan reduces the IgG interactions with Fc receptors (9). Thus aglycosylated and deglycosylated IgG1 have an abrogated or reduced propensity for binding to the FcγRs and C1q, but does not affect Fab antigen binding (10-13). Deglycosylated antibodies have been of interest to treat autoimmune disorders (14,15), and to suppress immune complex-mediated inflammation in a mouse arthritis model by disrupting Fc-Fc interactions, while maintaining intact antigen-antibody binding and complement binding (16). The deglycosylation of pathogen neuromyelitis optica anti-aquaporin-4 IgG in patients reduced its complement-dependent and antibody-dependent cell-mediated cytotoxicity with a reduction in antigen binding, giving it therapeutic potential (17).

Structural studies of IgG antibodies are crucial to understand their function. While many crystal structures are known for Fab regions, only one crystal structure is known for the full-length human IgG1 (PDB ID: 1HZH) (18), together with other full-length structures for two murine IgG subclasses (19). These crystal structures only provide a static view of full-length IgG1, and do not take into proper account a mobile and flexible hinge region, that allows for the independent movement of the Fab and Fc regions in solution (20). Crystal structures for glycosylated human Fc regions revealed the two glycans to be found at the centre of the Fc region in contact with each other (PDB IDs: 4W4N, 4KU1, 4BM7, 3AVE, 4Q74, 4BYH, 1H3X) (21-27). Crystal structures of the Fc region in complexes with the FcγRI and FcγRIII receptors showed similar modes of receptor binding to the upper part of the Fc region with many conserved contacts, despite their varying affinities to the Fc region (21,28,29). In these structures, very few contacts were found between the glycans and the FcγR, and there is no information on the full IgG1 structure after deglycosylation, making it unclear what role the glycans have. Nonetheless, crystal structures for deglycosylated Fc regions showed a more compact conformation of the C_H2 domains compared to the glycosylated Fc region, indicating that the glycans stabilise the Fc regions (27). In the deglycosylated Fc structures, the C'E loop (Gln^{293}-Phe^{303}) of the C_H2 domain that is involved in FcγR binding is more disordered (30). Previous solution studies of glycosylated and deglycosylated human Fc gave a larger radius of gyration R_G for deglycosylated Fc than that of glycosylated Fc (30). These studies suggest that Asn^{297} glycosylation is important to stabilise the open conformation of the C_H2 domains.

The effect of the Fc glycan chains on the full IgG structure is not well understood. To address this question, small angle X-ray and neutron scattering (SAXS, SANS) and analytical ultracentrifugation (AUC) were jointly applied to intact IgG1 as powerful solution structural

techniques for studying biological macromolecules. SAXS provides data sets measured in high positive solute-solvent contrast, in which the contribution of the hydrophilic surface regions of the glycoprotein are accentuated, while SANS measured with heavy water buffers provides data sets measured in high negative solute-solvent contrast, in which the contribution of the buried hydrophobic core of the glycoprotein is accentuated (31-33). The tightly-bound hydration layer is detected by SAXS because its electron density is similar to that of the protein and not to bulk water, while this same hydration layer is almost invisible by SANS measured in heavy water, because its nuclear density is almost the same as that of bulk water. The reproducibility of the two data sets corroborates the individual SAXS and SANS data sets because radiation effects in SAXS and aggregation in heavy water by SANS may perturb the output of either method. Their utility is much enhanced by the development of atomistic modelling of the SAXS and SANS data sets using molecular dynamics and Monte Carlo methods (34). Previous atomistic scattering modelling with glycosylated IgG1 revealed that IgG1 is conformationally stable, even in different buffer conditions, and exhibited an asymmetric IgG1 structure in which the arrangement of the Fab regions permitted the Fc region to bind to its FcγR and C1q ligands with no steric clashes (35,36). Here, we apply this joint SAXS-SANS-AUC approach together with atomistic modelling to show that deglycosylation does in fact result in a more flexible Fc structure within IgG1, in turn affecting the receptor-binding function of IgG1.

MATERIALS AND METHODS

Purification and composition of IgG1

IgG1 A33 (148 kDa) was generously supplied by Dr John O'Hara and Dr Berni Sweeney (UCB). Its enzymatic deglycosylation was performed using peptide:N-glycosidase F (PNGase F) (35.5 kDa; New England Biolabs, Massachusetts, USA) for reason of its ability to remove glycans completely from glycosylated Asn residues (37). To digest the glycans, 3.7 µl PNGase F (1850 activity units) was used to deglycosylate 150 µl IgG1 A33 (16.3 mg/ml). Native IgG1 was incubated at 37ºC for time points of 1 hour (TP1), 6 hours (TP6) and 10 hours (TP10). Each deglycosylated IgG1 sample was filtered, through three successive dilutions using Amicon Ultra-0.5 ml centrifugal filters (100 kDa cut-off), which simultaneously allowed the PNGase F to pass through the membrane, while concentrating the deglycosylated IgG1 sample. Immediately before SAXS, SANS or AUC measurements, glycosylated and deglycosylated IgG1 were purified by gel filtration to remove any non-specific aggregates using a Superose 6 Increase 10/300 GL column (Cytiva, Amersham, UK), then concentrated using Amicon Ultra-15 ml spin concentrators (100 kDa cut-off) and dialyzed at 4ºC into 20 mM L-histidine, 138 mM NaCl, and 2.6 mM KCl buffer, pH 6.0. This histidine buffer was found to increase the stability of IgG1. The sequence of IgG1 A33 was aligned against those for IgG1 19a, 6a and b12 (PDB ID: 1HZH), and an IgG1 Fc structure (PDB ID: 4W4N) (18,21,35) (Figure 2). The N-linked glycans at Asn^{297} on the C_H2 domains were assumed to be complex-type biantennary structures with a $Man_3GlcNAc_2$ core and two NeuNAc.Gal.GlcNAc antennae (4). From this sequence, the molecular mass of glycosylated IgG1 A33 was calculated to be 148.4 kDa, its unhydrated volume was 191.4 nm^3, its hydrated volume was 252.0 nm^3 (based on 0.3g of water/g of glycoprotein and an electrostricted volume of 0.0245 nm^3 per bound water molecule), its partial specific volume *v* was 0.731 ml/g and its absorption coefficient was 14.0 (1%, 1-cm pathlength, 280 nm) (31). The molecular mass of deglycosylated IgG1 A33 was 144.0 kDa, its unhydrated volume was 186.7 nm^3, its hydrated volume was 245.4 nm^3 , its partial specific volume *v* was 0.733 ml/g and its absorption coefficient was 14.4 (31). The X-ray and neutron scattering densities of glycan residues are similar to those for hydrophilic (polar) amino acid residues, these being slightly higher than those for hydrophobic (non-polar) amino acid residues (31). The buffer density was measured on an Anton Paar DMA 5000

density meter at 20°C to be 1.00578 g/ml in light water. In heavy water, the density was 1.11106 g/ml. Buffer viscosities were measured on an Anton Paar AMVn Automated microviscometer at 20°C. The viscosity in light water, pH 6.0, was 0.010190 poise.

The completeness of deglycosylation was verified by Superose 6 gel filtration, SDS-PAGE, and mass spectrometry. In the Mass Spectrometry Facility at the Chemistry Department University College London, the antibodies were analysed on an Agilent 6510 Quadrupole time-of-flight liquid chromatography mass spectrometry system (Agilent, UK). Ten µL of each sample was injected onto a PLRP-S, 1000A, 8 µM, 150 mm × 2.1 mm column, which was maintained at 60°C at a flow of 0.3 ml/min. The separation was achieved using mobile phase A (water with 0.1% formic acid) and B (acetonitrile, with 0.1% formic acid) using a gradient elution. The column effluent was continuously electrosprayed into the capillary electrospray ionization source of the Agilent 6510 QTOF mass spectrometer and electrospray ionization mass spectra were acquired in positive electrospray ionisation mode using the *m/z* range 1,000−3200 in profile mode. The raw data was converted to zero charge mass spectra using the maximum entropy deconvolution algorithm in the MassHunter software version B.07.00. The glycan masses were calculated by subtracting the mass of the full glycosylated IgG1 from the partially deglycosylated glycoform giving the mass of a single glycan chain. The single glycan mass was also found by subtracting the mass of fully glycosylated IgG1 from that for deglycosylated IgG1 and halving this mass.

Sedimentation velocity data and analysis for IgG1

Analytical ultracentrifugation data for native and deglycosylated IgG1 in light water at timepoints TP1, TP6 and TP10 were obtained on two Beckman XL-I instruments equipped with AnTi50 rotors. Data were collected at 20°C at a rotor speed of 40,000 rpm in two-sector cells with column heights of 12 mm for approximately 6 hours. Sedimentation analyses were performed using direct boundary Lamm fits of up to 896 scans using SEDFIT (version 15.01b) (38,39). SEDFIT resulted in size-distribution analyses *c(s)*, for which the algorithm assumes that all species have the same frictional ratio f/f_0. The final SEDFIT analyses (Table 1) used a fixed resolution of 200 and optimized the *c(s)* fits by floating f/f_0 and the baseline until the overall root mean square deviations and visual appearance of the fits were satisfactory. The percentage of oligomers in the total loading concentration was derived using the *c(s)* integration function. The observed *s* values were corrected to $s_{20,w}$ by:

$$s_{20,w} = s_{T,B}\left(\frac{\eta_{T,B}}{\eta_{20,w}}\right)\frac{(1-\bar{\nu}\rho)_{20,w}}{(1-\bar{\nu}\rho)_{T,B}}$$

where *s* is the sedimentation coefficient, the subscripts $_{T,B}$ refers to the temperature of the buffer. $_{20,w}$ refers to water at 20°C. ρ is the solvent density, η is the solvent viscosity and $\bar{\nu}$ is the protein partial specific volume.

X-ray and neutron scattering data and analyses for IgG1

X-ray scattering data were obtained during one beam session (October 2017) on Instrument B21 at the Diamond Light Source at the Rutherford Appleton Laboratory (Didcot, UK), operating with a ring energy of 3 GeV, and an operational energy of 12.4 keV. A PILATUS 2M detector with a resolution of 1475 × 1679 pixels (pixel size of 172 × 172 µm) was used with a sample-to-detector distance of 4.01 m giving a Q range from 0.04 nm^{-1} to 4 nm^{-1} (where $Q = 4\pi \sin\theta / \lambda$; 2θ = scattering angle; λ = wavelength). The glycosylated IgG1 (1.4-5.4 mg/ml) and the TP1 (0.7-4.9 mg/ml), TP6 (1.0-3.9 mg/ml) and TP10 (1.0-4.3 mg/ml) samples in light water were loaded onto a 96 well plate and placed into an EMBL Arinax

sample holder (40,41). This condition showed the antibody molecule as a hydrated structure in a high positive solute-solvent contrast (31). An automatic sampler injected 30 µl of sample from the well plate into a temperature-controlled quartz cell capillary with a diameter of 1.5 mm. Data sets of 30 frames with a frame exposure time of 1 second each were acquired in duplicate as a control of reproducibility. Checks during data acquisition confirmed the absence of radiation damage. ScÅtter (version 3.0) was used for buffer subtraction and data reduction, in which the 30 frames were averaged (42).

Neutron scattering data on glycosylated IgG1 (2.60-1.38 mg/ml) and the TP1 (4.78-2.32 mg/ml), TP6 (3.71-1.78 mg/ml) and TP10 (2.73-0.90 mg/ml) samples in heavy water were obtained in two sessions (March, October 2017) on instrument SANS2D at the ISIS pulsed neutron source at the Rutherford Appleton Laboratory (Didcot, UK) (43). This condition showed the antibody structure in a high negative solute-solvent contrast (31). No conformational differences in the antibody between light and heavy water were detected in this study or previously (36). A pulsed neutron beam was derived from proton beam currents of ~40 µA. SANS2D data were recorded with 4 m of collimation, a 4 m sample-to-detector distance, a 12 mm sample aperture, and a wavelength range of 0.175-1.65 nm made available by time of flight. This gave a Q range from 0.05 nm^{-1} to 4 nm^{-1}. The data were acquired using a two-dimensional ^{3}He detector with 512 × 512 pixels of 7.5 × 7.5 mm^2 in size. Samples of volume 1 ml were measured in 2 mm path length circular banjo cells for 1-7 h in a thermostated sample rack at 20°C. Data were reduced using MANTID software (44). The MANTID data reduction steps include corrections for the Q resolution, i.e. beam divergence effects and smearing from the shape and size of the slits, as well as the wavelength overlap in each pulse (44). Using SASview software, the Guinier analyses (below) were found to be almost unaffected if the smearing was turned on or off.

Guinier analyses of the scattering data gave information of the radius of gyration R_G, cross-sectional radius (R_{XS}) and molecular mass. The scattering curve $I(Q)$ intensities at low Q are defined by the R_G value which is the averaged distance of each scattering point from the centre of scattering. In a given solute-solvent contrast, the radius of gyration R_G is a measure of structural elongation if the internal inhomogeneity of scattering densities within the protein has no effect. Guinier analyses at low Q gave the R_G value and the forward scattering at zero angle $I(0)$ (45):

$$\ln I(Q) = \ln I(0) - \frac{{R_G}^2 Q^2}{3}$$

For antibodies, this expression is valid in a $Q.R_G$ range up to 1.5, and was used in our previous studies (35,36), although the usual upper range reported in the literature is 1.0-1.3. If the structure is elongated, the mean radius of gyration of the cross-sectional structure R_{XS} and the mean cross-sectional intensity at zero angle $[I(Q)Q]_{Q \longrightarrow 0}$ is obtained from (46):

$$\ln[I(Q)Q] = [I(Q)Q]_{Q \to 0} - \frac{{R_{XS}}^2 Q^2}{2}$$

For immunoglobulins, it has been long recognised that the cross-sectional plot exhibits two regions, a steeper innermost one and a flatter outermost one (46) and the two analyses are denoted by $R_{XS\text{-}1}$ and $R_{XS\text{-}2}$ respectively. The $R_{XS\text{-}1}$ parameter represents the averaged overall spatial separation of the Fab and Fc regions, while the $R_{XS\text{-}2}$ parameter represents the averaged spatial cross-section of the two Fab and one Fc region. The R_G and R_{XS} analyses were performed using SCT (Table 1) (47). The Q ranges for the R_G, $R_{XS\text{-}1}$ and $R_{XS\text{-}2}$ values were 0.10–0.22, 0.29–0.52, and 0.66–1.05 nm^{-1}, respectively, as previously (35,36). Indirect transformation of the

scattering data *I(Q)* in reciprocal space into real space to give the distance distribution function *P(r)* was carried out using GNOM (version 4.6) (48,49).

$$P(r) = \frac{1}{2\pi^2} \int_0^\infty I(Q) Qr \sin(Qr)\, dQ$$

P(r) corresponds to the distribution of distances *r* between the volume elements in the macromolecule. This yields the maximum dimension of the macromolecule *L* and its most commonly occurring distance vector *M* in real space. For this *P(r)* analysis, the X-ray *I(Q)* curve utilized up to 755 data points in the *Q* range between 0.032 and 1.70 nm^{-1} for both glycosylated and deglycosylated IgG1. The neutron *P(r)* curve utilized up to 155 *I(Q)* data points in the *Q* range between 0.055 and 1.60 nm^{-1} for both glycosylated and deglycosylated IgG1.

Atomistic modelling of IgG1

Starting structures were created for each of glycosylated and deglycosylated IgG1 A33 based on the A33 sequence provided by UCB. The latter was aligned with the sequences of IgG1 6a, IgG1 19a and IgG1 b12 (18,35) (Figure 2). This multiple sequence alignment was generated using Clustal Omega software (EMBL-EBI) (50). The Fab structure (Figure 1) was based on that found in the human IgG1 b12 crystal structure (PDB ID: 1HZH) (18) and the Fc structure was based on that for the rituximab IgG1 antibody Fc crystal structure (PDB ID: 4W4N) (21) which is unchanged from that of human IgG1 but is structurally complete compared to the IgG1 b12 structure where its Fc region showed gaps. Modeller (Version 9.19) (51) was used to generate the human IgG1 structure. In this, the IgG1 hinge was built using a PyMOL script build_seq (PyMOL Script Repository, Queen's University, Ontario, Canada), based on the sequence of ^{216}EPKSCDKTHTCPPCPAPELLGGP^{238}. The two N-linked oligosaccharides at Asn^{297} on the C_H2 domains were assumed to be complex-type biantennary oligosaccharide structures with a $Man_3GlcNAc_2$ core and two NeuNAc.Gal.GlcNAc antennae (4). The glycan template was taken from the GitHub repository (https://github.com/dww100), which was energy minimized using NAMD (52) for 1 nanosecond to achieve a relaxed structure. This glycan was added to the Fc region by bringing the C1 atom in the first GlcNAc residue to within 0.14 nm to the N sidechain atom of Asn^{297} in the C_H2 domain of IgG1, while ensuring no steric clashes with the Fc residues and the glycan chain. The PDB file was then opened on Discovery Studio (Dassault Systèmes BIOVIA, San Diego) where "CONECT" records were created for these glycosidic bonds. The CHARMM force field parameters and protein structure file (PSF), including those for the disulphide bridges and glycans were generated using the CHARMM-Gui GlycanReader tool (53-55) in order to be compatible with the CHARMM36 forcefield (54-58). To relax this structure, the full IgG1 structure with and without glycans were then energy minimised for 10,000 steps using the simulation engine NAMD version 2.9 with the CHARMM36 forcefield.

For the Monte Carlo simulations to generate trial structures, the starting IgG1 structure was renumbered and its naming nomenclature was adjusted to match the required format for the Torsion Angle Monte Carlo (TAMC) module on SASSIE-web (59). For TAMC to work, the IgG1 residue numbering was changed to be continuous for two segments, one segment corresponding to the first Fab region, its hinge and the Fc region, and the other segment to only the second Fab region and the hinge connected to this. A library of physically realistic glycosylated and deglycosylated structural conformations was generated by subjecting the starting structures to the TAMC module in SASSIE-web (59). The flexible regions were assigned within the hinge, namely ^{216}EPK^{218} and ^{231}APE^{233} on one side of IgG1, and just ^{216}EPK^{218} on the other side (Figures 1B, 2E). These tripeptides corresponded to surface-

accessible structures outside the structurally-defined Fab and Fc regions and the disulphide-linked hinge core. These tripeptides could be structurally varied to create the required IgG1 conformers for testing against the scattering curve. The rest of the IgG1 structure was held rigid. Making ^{216}EPK^{218} flexible on both sides of IgG1 rendered both Fab regions to be conformationally mobile, and making ^{231}APE^{233} flexible made the Fc region mobile. For each of these nine linker residues, the backbone phi (φ) and psi (ψ) torsion angles were varied in steps of up to either 30° or 180°. In the Monte Carlo simulation, many attempted moves will be physically unrealistic and were therefore discarded, For the glycosylated IgG1 simulations, 2,500,000 moves were attempted of which 123,284 were accepted. For the deglycosylated simulations, in which the glycan chains were omitted, 2,600,000 moves were attempted, of which 119,191 models were accepted.

For each of the 123,284 and 118,191 models, a scattering curve was generated using the SasCalc module in SASSIE-web. SasCalc calculates the scattering curve *I(Q)* using an all-atom expression for the scattering intensity in which the orientations of the *Q* vectors are taken from a quasi-uniform spherical grid generated by the golden ratio (60). For X-ray modelling, consideration of the hydration shell would require the explicit addition of a monolayer of water molecules to the protein surface before calculating *I(Q)*, and would require much computational effort (60). Thus the hydration shell was not considered here for X-rays, and was not required for neutrons. These scattering curves were compared to the X-ray and neutron experimental scattering curves, using the R-factor function in SASSIE-web. This function calculates the difference between the modelled curve $I_{Model}(Q_i)$ and the experimental curves $I_{Expt}(Q_i)$, this function being analogous to that used in protein crystallography:

$$R = \frac{\sum \left\| \|I_{Expt}(Qi)\| - \eta \, \|I_{Model}(Qi)\| \right\|}{\sum \|I_{Expt}(Qi)\|} \times 100$$

where Q_i is the Q value of the ith data point, $I_{Expt}(Q_i)$ is the experimental scattering intensity and $I_{Model}(Q_i)$ is the theoretical modelled scattering intensity, and η is a scaling factor used to match the theoretical curve to the experimental *I(0)* (47). Lower R-factor values represent better fits. An iterative search to minimize the R factor was used to determine η (47). In the extrapolated experimental scattering curves, the lowest *Q* values in the range before the fitted Guinier R_G region were interpolated to zero *Q* using MATLAB in order to satisfy the input requirement for the SasCalc module in SASSIE-web. Interpolation makes the *Q* spacing uniform between the data points, and extrapolation extends the full *I(Q)* curve to zero *Q*. The resulting 680 and 72 *I(Q)* values in the *Q* range of 0.0-1.5 nm^{-1} were utilised for the X-ray and neutron curve fits respectively, and defined the *Q* spacing for SasCalc and the R-factor values. The use of χ^2 analyses to evaluate the fits was not possible because this requires the experimental data points to have errors associated with them, which were not available when interpolating the curve. For the neutron curve fits, no correction was required for a flat incoherent background because the IgG1 concentrations were relatively low and dialyses had sufficiently reduced the proton content in the buffers. The 123,284 glycosylated and 119,191 deglycosylated models gave an R-factor vs. R_G distribution that encompassed the experimental extrapolated R_G value. This R-factor analysis was repeated for four experimental X-ray scattering curves at different concentrations for each of glycosylated and deglycosylated IgG1 (Table 2). The same analysis was repeated for two neutron scattering curves at different concentrations, for each of glycosylated and deglycosylated IgG1 (Table 3). For each concentration, the best-fit 100 models with the smallest R-factors were accepted.

Principal component analysis (PCA) provided by the Bio3d package in R (61) was used to identify the main classes of best-fit IgG1 conformations found in the 800 best-fit glycosylated and deglycosylated models from X-ray scattering (Table 2). A separate analysis of the 400 best-fit models from neutron scattering was performed. To remove any bias in the PCA clustering of coordinate sets caused by the presence or absence of the glycans, the glycan coordinates were removed from the best-fit glycosylated models prior to generating the PCA. The X-ray and neutron models were assessed through two separate PCA. The average structure for each PCA group was identified using a centroid model computed using R. The 100 best-fit glycosylated and deglycosylated IgG1 structures at 3.60 mg/ml and 4.29 mg/ml respectively are available to download in Supplementary Materials. The two single best-fit glycosylated and deglycosylated IgG1 structures were deposited in the SASBDB database (https://www.sasbdb.org/) with reference codes SAS2937 and SAS2938.

In order to model AUC parameters the theoretical $s_{20,w}$ values were generated for the best-fit 800 and 400 glycosylated and deglycosylated IgG1 models using HullRad Version 7 (62). Hullrad includes glycan residues for glycosylation, however there are inconsistencies in the Protein Database and CHARMM-GUI nomenclature for glycans. The nomenclature in the Hullrad script was thus modified to ensure that the IgG1 glycosylation was correctly incorporated in the $s_{20,w}$ calculation.

RESULTS

Purification and characterisation of glycosylated and deglycosylated IgG1

A protocol for the deglycosylation of the monoclonal human IgG1 A33 antibody was set up using peptide:N-glycosidase F (PNGase F) digests according to the manufacturer's protocol (Methods). The completeness of deglycosylation was verified by a combination of routine gel filtration, SDS-PAGE and mass spectrometry, and also by analytical ultracentrifugation (see below):

(i) At the timepoints of one hour, six hours and ten hours after the start of the digests (TP1, TP6 and TP10), the elution of the IgG1 digested products from a gel filtration column preceded that for native glycosylated IgG1 (Figure 3*A*). Both glycosylated and deglycosylated IgG1 eluted as a main symmetrical peak at 17.88 ml, 17.84 ml, 17.82 ml and 17.86 ml for glycosylated IgG1, and deglycosylated IgG1 at timepoints of TP1, TP6 and TP10, respectively (Figure 3*A*). This process ensured that the IgG1 sample was monodisperse with no aggregates present immediately before analytical ultracentrifugation or scattering experiments.

(ii) When the IgG1 samples were submitted to non-reducing and reducing SDS-PAGE analyses at equimolar concentrations, purified glycosylated and deglycosylated IgG1 showed a single band between 200 and 116kDa on 4-12% Bis Tris NuPage gel under non-reducing conditions, which is consistent with the expected masses of ~147 kDa for IgG1 (Figure 3*B*). Under reducing conditions two bands were present corresponding to the heavy chain (with an apparent mass of ~50 kDa) and the light chain (with an apparent molecular mass of ~25 kDa) (Figure 3*B*). These apparent molecular masses were as expected from the known sequence.

(iii) Liquid chromatography mass spectrometry measurements showed multiple peaks for glycosylated IgG1 (G) that were assigned to the presence of at least four glycoforms, separated by masses of 160-230 Da that corresponded to single sugar residues (Figure 3*C*) (63). The most intense IgG1 glycosylated population had an observed deconvoluted mass of 147,010 Da. After an hour of digest, a partially deglycosylated IgG1 (P) was observed in which the number of glycoforms was diminished, and additional peaks were observed at ~145.4 kDa and 143,958 Da. After six or ten hours, only the single dominant deglycosylated peak (D) was seen at 143,958 Da. The peak at 145.4 kDa was attributed to IgG1 in which one of the two glycans at Asn297 was not present. The mass of each glycan chain was calculated by subtracting the

glycosylated and deglycosylated masses and halving the outcome to give 1,526 Da. This glycan mass was also calculated by subtracting the glycosylated and half- deglycosylated masses to give 1613 Da. These values agree well with an assumed glycan composition of $Gal_2Man_3GlcNAc_4$ that gives a mass of 1622 Da.

Analytical ultracentrifugation of glycosylated and deglycosylated IgG1

Sedimentation velocity experiments investigated the masses and solution structures of glycosylated and deglycosylated IgG1 at the TP1, TP6 and TP10 timepoints. The SEDFIT analyses of the boundaries involved fits of as many as 896 scans, and the good agreement between the experimental boundary scans and fitted lines is clear (left, Figure 4*A*). In the resulting size distribution analyses *c(s)*, a monomer peak that monitored the overall IgG1 solution structure was observed at average $s_{20,w}$ values of 6.25 S for glycosylated IgG1, 6.12 S for IgG1 TP1, 6.15 S for IgG1 TP6, and 6.12 S for IgG1 TP10 (right, Figure 4*A*). For the glycosylated forms, these values agreed well with those of 6.42 S and 6.34 S for IgG1 6a and 19a respectively (35), and with earlier studies (64-66). From the *c(s)* analyses, the molecular masses of the IgG1 monomer peak were 151 kDa (glycosylated), 147 kDa (TP1), 156 kDa (TP6) and 148 kDa (TP10). These values agree well with the composition-calculated masses of 148.4 kDa and 144.4 kDa for the glycosylated and deglycosylated IgG1 monomers respectively. These also agree well with the values from mass spectrometry of 147,010 Da and 143,958 Da for glycosylated and deglycosylated IgG1 (Figure 3*C*). The 0.2 S reduction (3%) in the $s_{20,w}$ values on deglycosylation is attributable to the 4 kDa reduction (3%) in the IgG1 mass, according to the Svedberg equation in which $s_{20,w}$ is proportional to the mass divided by the frictional coefficient. This calculation assumes that the IgG1 conformation (i.e. the frictional coefficient) is unchanged after deglycosylation.

A slight concentration dependence was observed for the monomer $s_{20,w}$ values for glycosylated and deglycosylated IgG1 (Figure 4*B*), which increased with decreased concentration. In the 2015 study, minor peaks for IgG1 dimers were visible at about 9 S for IgG1 6a and 19a (35). In this work, no dimer peaks were visible for IgG1 A33 (right panel, Figure 4*A*). This difference may result from the use of histidine buffer in this current study, in distinction to the phosphate buffer saline used before. If IgG1 A33 forms dimers, the histidine buffer may have increased the exchange rate between monomer and dimer such that separate monomer and dimer peaks were no longer seen. Interestingly, the peak width for glycosylated IgG1 is greater than that of deglycosylated IgG1 (Figure 4*A*). The increased width may indicate a mix of monomer and dimer in fast exchange in glycosylated IgG1, which is reduced to monomer only upon deglycosylation.

X-ray and neutron scattering of glycosylated and deglycosylated IgG1

The overall solution structures of glycosylated and the three deglycosylated IgG1 samples at the TP1, TP6 and TP10 time points were analysed by X-ray and neutron scattering. The two methods provided slightly different perspectives of the same solution structure. X-rays in light water buffers detect the hydration shell surrounding the protein structure, whereas the effect of the hydration shell is reduced by neutrons in heavy water buffers for reason of the different solute-solvent contrast in use (31-33). The IgG1 X-ray data collection at concentrations between 0.5-5.5 mg/ml used time frame analyses to ensure the absence of radiation damage effects. The resulting R_G and $R_{XS\text{-}1}/R_{XS\text{-}2}$ values monitor the elongation of the overall IgG1 structure and its approximate cross-sectional structures respectively.

Guinier analyses resulted in high quality linear plots for all four samples and revealed three distinctive regions of the *I(Q)* curves, as expected for antibodies (35,67,68). From these,

the R_G, R_{XS-1} and R_{XS-2} values from the individual scattering curves were obtained within satisfactory $Q.R_G$ and $Q.R_{XS}$ limits of 0.5-1.4, 0.7-1.3 and 0.9-1.5 respectively (Figure 5*A*). A slight concentration dependence was observed in the X-ray *I(0)/c* values that suggested a small amount of oligomer formation in the concentration series (Figure 6*A*; Table 1). This agreed with the AUC data (Figure 4*B*). After extrapolation to zero concentration, the X-ray R_G values that monitor the overall structure for glycosylated IgG1, and the deglycosylated TP1, TP6 and TP10 IgG1 samples were almost unchanged at 5.10 ± 0.13 nm, 5.10 ± 0.20 nm, 5.11 ± 0.13 nm, and 5.13 ± 0.13 nm respectively. These X-ray R_G values for glycosylated IgG1 A33 here agree well with previous R_G values of 5.28 – 5.32 nm for two other human monoclonal IgG1 6a and 19a antibodies (35). The R_{XS-1} values from the individual curves (Figure 6*A*) is an approximate monitor of the cross-sectional structure for glycosylated IgG1 and deglycosylated IgG1. These were extrapolated to zero concentration to show that these were slightly increased from 2.47 ± 0.01 nm to 2.51 ± 0.01 nm respectively, showing some rearrangement between the Fab and Fc regions. The R_{XS-2} values from the individual curves for glycosylated IgG1 and deglycosylated IgG1 at the TP1, TP6 and TP10 timepoints were extrapolated to zero concentration to show that these were were almost unchanged at 1.40 ± 0.07 nm, 1.41 ± 0.05 nm, 1.41 ± 0.05 nm and 1.42 ± 0.04 nm. This showed that the individual Fab and Fc regions were unchanged in structure. In summary, the small increase of 0.04 nm in the extrapolated R_{XS-1} values with increasing deglycosylation suggested that there were small increases of elongation in the cross-sectional IgG1 structure upon removal of the glycan chains.

The corresponding neutron scattering data sets for glycosylated and deglycosylated IgG1 (TP1, TP6, TP10) in 100% ^2H_2O buffer were analysed at concentrations of 0.71-2.73 mg/ml, this concentration range being similar to that used above for SAXS. Again the Guinier analyses revealed high quality linear fits for the R_G, R_{XS-1} and R_{XS-2} parameters (Figure 5*B*). A concentration dependence was not observed for IgG1, this being seen from the *I(0)/c* values which remained unchanged within error (Figure 6*B*). This difference between the neutron and X-ray data sets is attributable to the fewer data points obtained with neutrons, leading to reduced precision in the data sets. The mean neutron R_G values for glycosylated IgG1 and deglycosylated IgG1 (TP1, TP6 and TP10) were unchanged at 5.27 ± 0.01 nm, 5.28 ± 0.06 nm, 5.28 ± 0.01 nm and 5.25 ± 0.06 nm respectively (Figure 6*B*). The neutron R_G values for glycosylated IgG1 A33 agree well with the R_G values of 5.16-5.18 nm for human IgG1 6a and 19a (35). The mean neutron R_{XS-1} values for glycosylated IgG1 and deglycosylated IgG1 (TP1, TP6 and TP10) were 2.35 ± 0.01 nm, 2.43 ± 0.01 nm, 2.42 ± 0.01 nm and 2.38 ± 0.01 nm respectively, suggesting a small increase in the cross-sectional structure following deglycosylation. The mean neutron R_{XS-2} values for glycosylated IgG1 and deglycosylated IgG1 (TP1, TP6 and TP10) were unchanged at 1.14 ± 0.04 nm, 1.19 ± 0.01 nm, 1.17 ± 0.01 nm and 1.15 ± 0.03 nm respectively. The neutron values confirmed the X-ray analyses.

The distance distribution function *P(r)* is derived from Fourier transformation of the scattering curve *I(Q)*, and provides structural information in real space on glycosylated and deglycosylated IgG1. The X-ray and neutron *P(r)* analyses gave R_G values that were similar to those from the X-ray Guinier analyses, showing that the two analyses were self-consistent (open symbols, Figure 6). The maximum lengths of glycosylated and deglycosylated IgG1 were determined from the value of *r* when the *P(r)* curve intersects zero on the *r* axis, and was 17 nm for all four IgG1 samples. The neutron maximum lengths of glycosylated and deglycosylated IgG1, were 16 nm for all four samples. These were 1 nm smaller when compared to the X-ray value of 17 nm, this being attributed to the reduced contribution of the hydration shell seen by neutron scattering (Figure 7*B*). These reductions in the neutron R_G and

L values have been previously seen in our earlier joint SAXS and SANS studies of antibodies (35).

The maxima in the *P(r)* curves corresponded to the most frequently occurring distances between scattering elements within the structures, these being a monitor of the IgG1 structure. For the four IgG1 samples, two peaks, *M1* and *M2*, were visible that are characteristic of antibody-shaped proteins. *M1* corresponds primarily to the shorter distances within each Fab and Fc region, and is expected to be almost invariant for this reason. *M2* corresponds primarily to the longer distances between pairs of Fab and Fc regions and monitors changes in the separation of the Fab and Fc regions (Figures 1 and 7). No concentration dependence was observed in the positions of the *M1* and *M2* peaks, which were measured directly from their maximum values (Figures 7*B,C*). However, the X-ray *M2* peak shifted significantly from a mean value of 7.44 ± 0.03 nm for glycosylated IgG1 to a mean value of 7.83 ± 0.02 nm for deglycosylated IgG1 (Figure 7*C*). The X-ray *M1* peak shifted much less from 4.42 ± 0.02 nm for glycosylated IgG1 to 4.49 ± 0.01 nm for deglycosylated IgG1. The same change was seen in the neutron *P(r)* curves, when *M2* increased from 7.27 ± 0.22 nm for glycosylated IgG1 to 7.77 ± 0.04 nm for deglycosylated IgG1 (Figure 7*D*). The neutron *M1* peak was almost unchanged, with a shift from 4.36 ± 0.07 nm for glycosylated IgG1 to 4.21 ± 0.048 nm for deglycosylated IgG1. Both the X-ray and neutron analyses were consistent with each other.

Atomistic modelling of glycosylated and deglycosylated IgG1

In order to account for the changes seen in the $R_{XS\text{-}1}$ and *M2* scattering parameters in IgG1 following deglycosylation, atomistic modelling simulations of the glycosylated and deglycosylated structures were performed, starting from two high-resolution crystal structures for the human Fab and Fc regions (Materials and Methods). The sequence in the Fab structure was converted into that for IgG1 A33 using Modeller (Figure 2*A-D*). The Fab and Fc regions were joined by a peptide ^{216}EPKSCDKTHTCPPCPAPELLGGP^{238} that included the 15-residue hinge sequence (Figure 2*E*), also built using Modeller. The native glycosylated IgG1 models were created by adding complex-type biantennary glycans to the two Asn^{297} sidechains in the Fc region (Figure 1*B*). This starting structure was subjected to energy minimisation.

Physically-realistic IgG1 models without steric overlaps or clashes were created for comparison with the experimental X-ray curves. By varying the torsion angles at three flexible regions at the start and end of the two IgG1 hinges (Materials and Methods)(Figure 1), trial IgG1 structures were created that involved movements of the two Fab and one Fc regions relative to each other. For glycosylated IgG1, 2,500,000 models were generated in 16 Monte Carlo simulations, from which 123,284 models were accepted because these showed no steric clashes between separate residues in the model. For deglycosylated IgG1, 2,600,000 models were generated in 20 Monte Carlo simulations, of which 119,191 models were likewise acceptable. To ensure that no systematic trends were overlooked in the modelling outcome, four X-ray and two neutron scattering curves from up to four concentrations were fitted for each of the four samples in question (Figure 8). For both glycosylated and deglycosylated IgG1, comparison of the four experimental X-ray scattering curves at 1.36-3.60 mg/ml with the 123,284 and 119,191 theoretical curves gave a goodness-of-fit *R*-factor vs R_G distribution with clear minima in all eight cases (Figure 8*A,B*). The minima agreed with the experimental R_G values (Figure 6*A*). The minima showed that enough trial X-ray models had been generated to result in good fits in each case. Filtering of the models to select these with the lowest *R* -factors gave the 100 best-fit models for each concentration (red, Figure 8). The range of the 100 *R*-factors for each of the four concentrations was low at between 0.80-1.93% for the best-fit

glycosylated models and 0.70-2.18% for the best-fit deglycosylated models (Table 2). This indicated good quality X-ray curve fits between the experimental and modelled curves.

The eight sets of 100 best-fit models (Figure 8) were examined in order to identify the resulting best-fit IgG1 conformations from the curve fits. For this, principal component analyses (PCA) were performed (69). The PCA determines the correlated motions of protein residues as linearly uncorrelated variables, each being termed a principal component (69). These "essential motions" were extracted from a covariance matrix of the atomic coordinates of the frames in the selected structure set. The eigenvectors of this matrix each have an associated eigenvalue that characterises the clustering of the models based on structural coordinates (or variance). In order to eliminate bias in the PCA, the glycan chains were removed from the glycosylated IgG1 models before comparison with the deglycosylated models. The PCA confirmed a clear difference between the glycosylated and deglycosylated X-ray IgG1 models (black and magenta respectively, Figure 9*A-D*; Table 2). Thus the distributions of the best-fit 400 glycosylated and 400 deglycosylated X-ray models were each clustered into five distinct groups, with little overlap between glycosylated and deglycosylated groups. The glycosylated models mostly occurred in the PCA Groups 1, 2 and 3, while the deglycosylated models mostly occurred in the PCA Groups 4 and 5. This outcome verified the experimentally-observed changes in the $R_{XS\text{-}1}$ and *M2* parameters before and after deglycosylation (Figures 6*A*, 7*C*). The visually-excellent X-ray curve fits confirmed the validity of the modelling fits (Figures 10*A,B*). Of particular note was the agreement of the experimental and theoretical double peaks in the *P(r)* curves shown as insets.

The same outcome was found with the theoretical neutron modelling and PCA, thus confirming the reproducibility of the curve fits, although the precision of the neutron scattering curves was reduced. The same 123,284 and 119,191 theoretical curves were compared with the neutron scattering curves at 0.90-2.73 mg/ml to show again that 100 best-fit structures could be identified at clear minima in each of the *R*-factor vs R_G neutron distributions (Figures 8*C*, 8D). The neutron PCA also indicated clear differences between the glycosylated and deglycosylated neutron IgG1 models (black and magenta respectively, Figure 9*E-H*; Table 3). The distributions of the best-fit 200 glycosylated and 200 deglycosylated neutron models were each again clustered into two major groups 1 and 4, and three more less populated groups, with little overlap between glycosylated and deglycosylated groups. The glycosylated models mostly occurred in the PCA Group 1, while the deglycosylated models mostly occurred in the PCA Group 4. Visually-excellent neutron curve fits were obtained (Figures 10*C,D*).

Further insights into the X-ray and neutron data and their modelling were obtained from the dimensionless Kratky analyses of $(Q.R_G)^2.I(Q)/I(0)$ *vs* $Q.R_G$ for the experimental scattering curves at the highest concentrations in use and the scattering curves from the modelled best fit structures. These plots indicate whether the macromolecule in question is globular in its structure or possesses intrinsically disordered regions (70). The Kratky plots all demonstrated two clear peaks in both the experimental and theoretical modelled curves. For the X-ray Kratky curves (Figure 11*A*), the $Q.R_G$ values for the experimental glycosylated peaks were 1.96 and 4.05, in good accord with the modelled values of 1.93 and 3.98. The $Q.R_G$ values for the experimental deglycosylated peaks of 2.01 and 4.15 were also in good accord with the modelled deglycosylated peaks of 1.97 and 4.08. It was interesting to note that the second peak showed higher intensities for deglycosylated IgG1 (magenta) than for glycosylated IgG1 (black), suggesting that there was a small increase in antibody disorder after deglycosylation. For the SANS Kratky curves (Figure 11*B*), the $Q.R_G$ values for the experimental peaks for glycosylated IgG1 were 2.45 and 4.68, which were similar to the modelled peaks at 1.99 and

4.43. The $Q.R_G$ values for the experimental peaks for deglycosylated IgG1 were 1.91 and 5.16, but showed less agreement for the modelled peaks at 1.91 and 4.37. Again the second neutron peak showed higher intensities for deglycosylated IgG1 (magenta) when compared with glycosylated IgG1 (black), suggesting that a greater disorder was present after deglycosylation.

As another test of the scattering modelling, the $s^0_{20,w}$ values for the eight sets of best-fit 100 glycosylated and deglycosylated models from each X-ray concentration (Figures 8, 10) were calculated using HullRad (62). This gave an $s^0_{20,w}$ range of 6.57-6.77 S for the four X-ray concentrations for glycosylated IgG1 and 6.24-6.50 S for deglycosylated IgG1 (Table 2). These values agreed well with the experimental $s^0_{20,w}$ values of 6.16-6.43 S for glycosylated IgG1 and 6.09-6.15 S for deglycosylated IgG1 (Table 1). These agreements corroborated the outcome of the atomistic scattering modelling, given that the mean difference between the modelled and experimental values should typically be ±0.21 S for related macromolecules (71). This modelling was however unable to distinguish changes before and after deglycosylation.

DISCUSSION

This scattering and atomistic modelling study has notably clarified the conformational effect of removing the two glycans chains on the structure of the major IgG1 antibody subclass. Unlike earlier protein structural investigations based on crystallography, NMR or circular dichroism (CD), our approach provided a more informative outcome on full-sized IgG1 of the changes accompanying deglycosylation of the two conserved Asn^{297} residues in the Fc region (Figure 1*B*). The complete deglycosylation of IgG1 was validated by a combination of gel filtration, routine mass spectrometry, and AUC. The AUC data showed that the IgG1 samples were monomeric and showed a slight concentration dependence in the $s_{20,w}$ values that were extrapolated to give the $s^0_{20,w}$ values. Subsequently, the glycosylated and deglycosylated IgG1 proteins were submitted to abundant SAXS and SANS data collection to establish their Guinier R_G, R_{XS-1} and R_{XS-2} values, and their distance distribution curves *P(r)*. Small changes in the R_{XS-1} values and larger changes in the *M2* parameter that monitored the mean separation of the Fab and Fc regions in IgG1 were seen on deglycosylation. The advent of atomistic scattering modelling using SASSIE (34) based on molecular dynamics and Monte Carlo simulations gave excellent curve fits based on large stereochemically-correct trial conformational libraries for IgG1. The display and interpretation of the output was much facilitated by PCA analyses. Two different conformational best-fit structures for glycosylated and deglycosylated IgG1 were identified by PCA. The clearest view of the final result was determined from wireframe representations of the 100 best fit structures (Figure 12). Views of the 100 best-fit X-ray models at four concentrations showed that the glycosylated Fc region occupied a smaller volume (blue wirefame, Figure 12*A*) than the notably larger volume occupied by the deglycosylated Fc regions (magenta wireframe, Figure 12*A*). This outcome showed that the Fab and Fc regions formed better defined native glycosylated structures compared to the more dispersed and flexible structures seen after deglycosylation. The 100 best-fit neutron models were limited by the reduced precision of the neutron scattering data, but are consistent with this interpretation (Figure 12*B*). The Kratky plots also suggest greater disorder following deglycosylation (Figure 11), in keeping with the flexibility shown in Figure 12*A*.

Our results (Figure 12*A*) account for previous functional studies of human IgG1. The Fc region of IgG1 is responsible for interactions with the three classes of human Fcγ receptors (FcγRs) and with the globular heads of human C1q. Several studies have reported that both interactions are abrogated following deglycosylation. Thus the antibody effector functions such as antibody-dependent cytotoxicity and complement dependent cytotoxicity mediated by FcγRs and C1q are impaired for aglycosylated and deglycosylated antibodies (27,72,73).

Deglycosylated IgG1 was used as a negative control in surface plasmon resonance experiments in which several FcγRs were tested, and deglycosylated IgG1 failed to bind to these with the exception of the high affinity FcγRI (74). Our structural investigations explains these findings by showing that the orientation of the Fc region in IgG1 has become disorganised (Figure 12*A*). The cartoon view (Figure 12*C*) showed that the deglycosylated Fc region occupied more conformational space than the glycosylated one. High-resolution crystal structures of glycosylated Fc regions bound to the FcγRs showed none or little interaction with the Fc glycan chains, and receptor binding generally occured at residues in the lower hinge (21,75-77). Accordingly, from our work, IgG1 deglycosylation means that the essential presentation of structurally well-defined C_H2 domain surfaces in the Fc region near the hinge peptides is no longer present. It follows from this conclusion that the glycoengineering of human IgG1 based on either the removal or modification of specific glycosylation patterns in the two Fc glycans will influence receptor binding and in turn the effector functions if human IgG1, such as its core fucosylation (78-80) and terminal sialic acids (81).

The advantage of our combined SAXS-SANS-AUC-MC approach is the ability to address the full IgG1 structure, this being the functional native structure. Previous structural studies have focussed on the Fc region alone, because it is difficult to crystallise the full IgG1 antibody compared to the Fc region alone, and NMR and circular dichroism studies are more difficult with the full IgG1 structure because its molecular mass has tripled to over 150 kDa. Previous NMR solution studies of the glycosylated and deglycosylated Fc region (82) showed that the glycan chain at Asn^{297} stabilises the loop between β-strands C' and E in the C_H2 domains, and in turn positions the two C_H2 domains into a stable orientation seen in 22 Fc crystal structures to orient the FcγR interface on the Fc region for optimal binding affinity with receptors. Previous crystallography studies of the deglycosylated Fc region showed that the C_H2 domains had reorientated themselves to form a more compact structure. (30). Circular dichroism solution studies of the glycosylated and deglycosylated Fc region studied the β-sheet secondary structure of its four domains (Figure 1) (83). By this, similar β-sheet rich structures showing a minimum at 217 nm were observed for both forms of the Fc region, showing that this β-sheet structure was preserved with or without the glycan chains. The greater mobility of the Fc region following glycan removal, as observed in this study (Figure 12*A*), would not have been observed by circular dichroism. These previous studies on the Fc region alone complement our results showing that the Fc region within intact IgG1 is more flexible after deglycosylation.

The advent of atomistic scattering modelling has resulted in a molecular explanation of the changes induced in IgG1 following glycan removal. Traditionally solution scattering is a low resolution method with a resolution of around 2 nm, while protein crystallography routinely achieves resolutions that are over ten times better. Our recent IgG1 modelling analysis used "constrained" modelling based on the Fab and Fc crystal structures and joined by a hinge region that was conformationally randomised using molecular dynamics to give 20,000 trial models (35). Seven different fits from X-ray and neutron data out to Q values of 1.5 nm^{-1} for human IgG1 6a and 19a in different NaCl buffers corresponded to clear minima in the R-factor vs. R_G graphs. All these revealed an asymmetric solution structure for IgG1, in agreement with the single asymmetric conformation seen in the crystal structure of human IgG1 b12 (18), and that for glycosylated IgG1 from SasCalc (Figure 12). The best-fit R-factors were 2.8-3.7%. This conformation permitted the Fc region to bind readily to its FcγR and C1q ligands without steric clashes. The follow-up study on human IgG1 using "atomistic" scattering modelling involved further X-ray and neutron data collection out to Q values of 1.5 nm^{-1}, and fitting these data to 231,492 trial models produced from full molecular dynamics and rapid

Monte Carlo simulations (36). The best-fit R-factors were 2.9%. This improved method likewise gave an asymmetric IgG1 solution structure similar to that seen in the crystal structure of human IgG1 b12 (18), and also that for glycosylated IgG1 from SasCalc (Figure 12). This likewise accounted for the binding of the Fc region to its FcγR and C1q ligands. Of particular interest is that the previous use of the SCT/SCTPL modelling approach (available in SASSIE-web) had explicitly incorporated hydration shells in a coarse-grained approach (47). The current atomistic modelling study using SasCalc (60) did not include atomistic representation of hydration shells because this is computationally expensive. The final outcomes from all three X-ray modellings were similar, when all three showed asymmetric IgG1 solution structures. In the present study, the simulations of IgG1 A33 were based on X-ray and neutron data that extended out to Q values of 1.5 nm^{-1} and resulted in fits with low R-factors of 1% or less (Table 2). This R-factor improvement is attributed to the improved signal-noise ratio of the scattering curves from the B21 instrument at Diamond. The atomistic modelling approach in combination with high quality SAXS data with little noise at large Q values has been of great value in studying structural perturbations in IgG antibodies caused by the removal of its two glycans.

SUPPORTING MATERIAL

The experimental scattering curves and the coordinates of our final best-fit models are available at the Biophysical Journal website (to be confirmed).

AUTHOR CONTRIBUTIONS

V.A.S. obtained AUC, SAXS and SANS data and analysed these, performed the modelling analyses, and wrote the paper. J.D., R.P.R and J.G. assisted with the SANS, SAXS and AUC data collection respectively. P.A.D. supervised the work. S.J.P. conceived and coordinated the study, supervised the work, and wrote the paper. The authors declare that they have no conflicts of interest with the contents of this article.

ACKNOWLEDGEMENTS

V.A.S. was supported by an EPSRC Centre for Doctoral Training in Emergent Macromolecular Therapies (EP/L015218/1), Diamond Light Source Ltd. (STU0174), and ISIS neutron facility joint PhD studentship. S.J.P. was supported by a joint EPSRC (EP/K039121/1) and NSF (CHE01265821) grant for CCP-SAS. We thank UCB for donating IgG1 A33 antibodies. We thanks Dr Nathan Cowieson, Dr Katsuaki Inoue and Mr Nikul Khunti for user support on Instrument B21 at Diamond. We thank Dr Gar Kay Hui, Dr Amy J. Osborne, Dr Jayesh S. Bhatt, and Dr Joseph E. Curtis for excellent computational support and useful discussions. We thank Ms Malgorzata Puchnarewicz and Dr Kersti Karu for mass spectrometry measurements in the UCL Department of Chemistry Mass Spectrometry Facility.

REFERENCES

1. Vidarsson, G., Dekkers, G. & Rispens, T. (2014). IgG subclasses and allotypes: From structure to effector functions. Frontiers in Immunology, 5, 1–17. https://doi.org/10.3389/fimmu.2014.00520
2. Hamilton, R. G. (1987). Human IgG subclass measurements in the clinical laboratory. Clinical Chemistry, 33, 1707–1725.
3. Reichert, J. M. (2020). Therapeutic monoclonal antibodies approved or in review in the EU or the US. The Antibody Society. Retrieved February 17, 2020, from https://www.antibodysociety.org/resources/approved-antibodies/

4. Deisenhofer, J. (1981). Crystallographic Refinement and atomic models of a human Fc fragment and its complex with Fragment B of Protein A from Staphylococcus aureus at 2.9- and 2.8-Å resolution. Biochemistry, 20, 2361–2370. https://doi.org/10.1021/bi00512a001
5. Wuhrer, M., Stam, J. C., van de Geijn, F. E., Koeleman, C. A. M., Verrips, C. T., Dolhain, R. J. E. M., Hokke, C. H. & Deelder, A. M. (2007). Glycosylation profiling of immunoglobulin G (IgG) subclasses from human serum. Proteomics, 7, 4070–4081. https://doi.org/10.1002/pmic.200700289
6. Martin, W. L., West, A. P., Gan, L. & Bjorkman, P. J. (2001). Crystal structure at 2.8 Å of an FcRn/heterodimeric Fc complex: Mechanism of pH-dependent binding. Molecular Cell, 7, 867–877. https://doi.org/10.1016/S1097-2765(01)00230-1
7. Shields, R. L., Lai, J., Keck, R., O'Connell, L. Y., Hong, K., Meng, Y.G., Weikert, S. H. & Presta, L. G. (2002). Lack of fucose on human IgG1 N-linked oligosaccharide improves binding to human FcγRIII and antibody-dependent cellular toxicity. J. Biol. Chem. 277, 26733–26740. https://doi.org/10.1074/jbc.M202069200
8. Pereira, N. A., Chan, K. F., Lin, P. C. & Song, Z. (2018). The "less-is-more" in therapeutic antibodies: Afucosylated anti-cancer antibodies with enhanced antibody-dependent cellular cytotoxicity. mAbs, 10, 1–44. https://doi.org/10.1080/19420862.2018.1466767
9. Jefferis, R. (2007). Antibody therapeutics: isotype and glycoform selection. Expert Opin. Biol. Therapy, 7, 1401–1413. https://doi.org/10.1517/14712598.7.9.1401
10. Nose, M. & Wigzell, H. (1983). Biological significance of carbohydrate chains on monoclonal antibodies. Proc. Natl. Acad.Sci. U.S.A. 80, 6632–6636. https://doi.org/10.1073/pnas.80.21.6632
11. Pound, J. D., Lund, J. & Jefferis, R. (1993). Aglycosylated chimaeric human IgG3 can trigger the human phagocyte respiratory burst. Molecular Immunology, 30, 233–241. https://doi.org/10.1016/0161-5890(93)90052-D
12. Radaev, S. & Sun, P. D. (2001). Recognition of IgG by Fcγ Receptor: The role of Fc glycosylation and the binding of peptide inhibitors. J. Biol. Chem. 276, 16478–16483. https://doi.org/10.1074/jbc.M100351200
13. Lu, J. & Sun, P. D. (2015). Structural mechanism of high affinity FcγRI recognition of immunoglobulin G. Immunol. Rev. 268, 192–200. https://doi.org/10.1111/imr.12346
14. Crispin, M. (2013). Therapeutic potential of deglycosylated antibodies. Proc. Natl. Acad.Sci. U.S.A., 110, 10059–10060. https://doi.org/10.1073/pnas.1307776110
15. Collin, M., Shannon, O. & Björck, L. (2008). IgG glycan hydrolysis by a bacterial enzyme as a therapy against autoimmune conditions. Proc. Natl. Acad.Sci. U.S.A. 105, 4265–4270. https://doi.org/10.1073/pnas.0711271105
16. Nandakumar, K. S., Collin, M., Happonen, K. E., Croxford, A. M., Lundström, S. L., Zubarev, R. A., … Holmdahl, R. (2013). Dominant suppression of inflammation by glycan-hydrolyzed IgG. Proc. Natl. Acad.Sci. U.S.A., 110, 10252–10257. https://doi.org/10.1073/pnas.1301480110
17. Tradtrantip, L., Ratelade, J., Zhang, H. & Verkman, A. S. (2013). Enzymatic deglycosylation converts pathogenic neuromyelitis optica anti-aquaporin-4 immunoglobulin G into therapeutic antibody. Ann. Neurology, 73, 77–85. https://doi.org/10.1002/ana.23741
18. Saphire, E. O., Parren, P. W. H. I., Pantophlet, R., Zwick, M. B., Morris, G. M., Rudd, P. M., Dwek, R. A., Stanfield, R. L., Burton, D. R. & Wilson, I. A. (2001). Crystal structure of a neutralizing human IgG against HIV-1: A template for vaccine design. Science, 293, 1155–1159. https://doi.org/10.1126/science.1061692
19. Harris, L. J., Skaletsky, E. & McPherson, A. (1995). Crystallization of intact monoclonal

antibodies. Proteins: Struct. Funct. Bioinf. 23, 285–289. https://doi.org/10.1002/prot.340230218
20. Jefferis, R. (2012). Isotype and glycoform selection for antibody therapeutics. Arch. Biochem. Biophys. 526, 159–166. https://doi.org/10.1016/j.abb.2012.03.021
21. Kiyoshi, M., Caaveiro, J. M. M., Kawai, T., Tashiro, S., Ide, T., Asaoka, Y., Hatayama, K. & Tsumoto, K. (2015). Structural basis for binding of human IgG1 to its high-affinity human receptor FcγRI. Nature Comm. 6, 1–11. https://doi.org/10.1038/ncomms7866
22. Frank, M., Walker, R. C., Lanzilotta, W. N., Prestegard, J. H. & Barb, A. W. (2014). Immunoglobulin G1 Fc Domain Motions: Implications for Fc Engineering. J. Mol. Biol. 426, 1799–1811. https://doi.org/10.1016/j.jmb.2014.01.011
23. Yu, X., Baruah, K., Harvey, D. J., Vasiljevic, S., Alonzi, D. S., Song, B. D., Higgins, M. K., Bowden, T. A., Scanlan, C. N. & Crispin, M. (2013). Engineering hydrophobic protein-carbohydrate interactions to fine-tune monoclonal antibodies. J. Am. Chem. Soc. 135, 9723–9732. https://doi.org/10.1021/ja4014375
24. Matsumiya, S., Yamaguchi, Y., Saito, J., Nagano, M., Sasakawa, H., Otaki, S., Satoh, M. Shitara, K. & Kato, K. (2007). Structural comparison of fucosylated and nonfucosylated Fc fragments of human immunoglobulin G1. J. Mol. Biol. 368, 767–779. https://doi.org/10.1016/j.jmb.2007.02.034
25. Ahmed, A. A., Giddens, J., Pincetic, A., Lomino, J. V., Ravetch, J. V., Wang, L.-X. & Bjorkman, P. J. (2014). Structural characterization of anti-inflammatory immunoglobulin G Fc proteins. J. Mol. Biol. 426, 3166–3179. https://doi.org/10.1016/j.jmb.2014.07.006
26. Crispin, M., Yu, X. & Bowden, T. A. (2013). Crystal structure of sialylated IgG Fc: Implications for the mechanism of intravenous immunoglobulin therapy. Proc. Natl. Acad.Sci. U.S.A., 110, 3544–3546. https://doi.org/10.1073/pnas.1310657110
27. Krapp, S., Mimura, Y., Jefferis, R., Huber, R. & Sondermann, P. (2003). Structural analysis of human IgG-Fc glycoforms reveals a correlation between glycosylation and structural integrity. J. Mol. Biol. 325, 979–989. https://doi.org/10.1016/S0022-2836(02)01250-0
28. Sondermann, P., Huber, R., Oosthuizen, V. & Jacob, U. (2000). The 3.2-A crystal structure of the human IgG1 Fc fragment-FcγRIII complex. Nature, 406, 267–273. https://doi.org/10.1038/35018508
29. Radaev, S., Motyka, S., Fridman, W. H., Sautes-Fridman, C. & Sun, P. D. (2001). The Structure of a Human Type III Fcγ Receptor in Complex with Fc. J. Biol. Chem. 276, 16469–16477. https://doi.org/10.1074/jbc.M100350200
30. Borrok, M. J., Jung, S. T., Kang, T. H., Monzingo, A. F. & Georgiou, G. (2012). Revisiting the role of glycosylation in the structure of human IgG Fc. ACS Chem Biol, 7, 1596–1602. https://doi.org/10.1021/cb300130k.
31. Perkins, S. J. (1986). Protein volumes and hydration effects. The calculations of partial specific volumes, neutron scattering matchpoints and 280-nm absorption coefficients for proteins and glycoproteins from amino acid sequences. Eur. J. Biochem. 157, 169–80. http://www.ncbi.nlm.nih.gov/pubmed/3709531
32. Perkins, S. J. (2001). X-Ray and neutron scattering analyses of hydration shells: A molecular interpretation based on sequence predictions and modelling fits. Biophys. Chem. 93, 129–139. https://doi.org/10.1016/S0301-4622(01)00216-2
33. Svergun, D.I., Richard, S., Koch, M.H., Sayers, Z., Kuprin, S. & Zaccai G. (1998). Protein hydration in solution: experimental observation by X-ray and neutron scattering. Proc. Natl. Acad. Sci. U. S. A. 95, 2267-2272. DOI: 10.1073/pnas.95.5.2267
34. Perkins, S. J., Wright, D. W., Zhang, H., Brookes, E. H., Chen, J., Irving, T. C., Krueger, S., Barlow, D. J., Edler, K. J., Scott, D. J., Terrill, N. J., King, S. M., Butler, P. D &

Curtis, J. E. (2016). Atomistic modelling of scattering data in the ollaborative Computational Project for Small Angle Scattering (CCP-SAS). J. Appl. Cryst. 49, 1861–1875. https://doi.org/10.1107/S160057671601517X
35. Rayner, L. E., Hui, G. K., Gor, J., Heenan, R. K., Dalby, P. A. & Perkins, S. J. (2015). The solution structures of two human IgG1 antibodies show conformational stability and accommodate their C1q and FcγR ligands. J. Biol. Chem. 290, 8420–8438. https://doi.org/10.1074/jbc.M114.631002
36. Wright, D. W., Elliston, E. L. K., Hui, G. K. & Perkins, S. J. (2019). Atomistic modeling of scattering curves for human IgG1/4 reveals new structure-function insights. Biophys. J. 117, 2101–2119. https://doi.org/10.1016/j.bpj.2019.10.024
37. Plummer, T. H., Elder, J. H., Alexander, S., Phelan, A. W. & Tarentino, A. L. (1984). Demonstration of peptide:N-glycosidase F activity in endo-beta-N-acetylglucosaminidase F preparations. J. Biol. Chem. 259, 10700–10704. http://www.ncbi.nlm.nih.gov/pubmed/6206060
38. Schuck, P. (1998). Sedimentation analysis of noninteracting and self-associating solutes using numerical solutions to the Lamm equation. Biophys. J. 75, 1503–1512. https://doi.org/10.1016/S0006-3495(98)74069-X
39. Schuck, P. (2000). Size-distribution analysis of macromolecules by sedimentation velocity ultracentrifugation and Lamm equation modeling. Biophys. J. 78, 1606–1619. https://doi.org/10.1016/S0006-3495(00)76713-0
40. Pernot, P., Round, A., Barrett, R., De Maria Antolinos, A., Gobbo, A., Gordon, E., Huet, J., Kieffer, J., Lentini, M., Mattenet, M., Morawe, C., Mueller-Diekemann, C., Ohlsson, S., Schmid, W., Surr, J., Theveneau, P., Zerrad, L. & McSweeney, S. (2013). Upgraded ESRF BM29 beamline for SAXS on macromolecules in solution. J. Synchrotron Rad. 20, 660–664. https://doi.org/10.1107/S0909049513010431
41. Round, A., Felisaz, F., Fodinger, L., Gobbo, A., Huet, J., Villard, C., Blanchet, C. E., Pernot, P., McSweeney, S., Roessle, M., Svergun, D. I. & Cipriani, F. (2015). BioSAXS sample changer: A robotic sample changer for rapid and reliable high-throughput X-ray solution scattering experiments. Acta Cryst. D71, 67–75. https://doi.org/10.1107/S1399004714026959
42. https://www.diamond.ac.uk/Instruments/Soft-Condensed-Matter/small-angle/B21.html
43. Heenan, R. K., Rogers, S. E., Turner, D., Terry, A. E., Treadgold, J. & King, S. M. (2011). Small angle neutron scattering using SANS2d. Neutron News, 22, 19–21. https://doi.org/10.1080/10448632.2011.569531
44. Arnold, O., Bilheux, J. C., Borreguero, J. M., Buts, A., Campbell, S. I., Chapon, L., Doucet, M., Draper, N., Ferraz Leal, R., Gigg, M. A., Lynch, V. E., Markvardsen, A., Mikkelson, D. J., Mikkelson, R. L., Miller, R., Palmen, K., Parker, P., Passos, G., Perring, T. G., Peterson, P. F., Ren, S., Reuter, M. A., Savici, A. T., Taylor, J. W., Taylor, R. J., Tolchenov, R., Zhou W. & Zikovsky, J. (2014). Mantid - Data analysis and visualization package for neutron scattering and μ SR experiments. Nucl. Inst. Meth. Phys. Res. A764, 156–166. https://doi.org/10.1016/j.nima.2014.07.029
45. Glatter, O. & Kratky, O. Eds. (1982). Small Angle X-ray scattering. New York: Academic Press.
46. Pilz, I., Puchwein, G., Kratky, O., Herbst, M., Haager, O., Gall, W. E. & Edelman, G. M. (1970). Small angle X-ray scattering of a homogeneous γG1 immunoglobulin. Biochemistry, 9, 211–219. https://doi.org/10.1021/bi00804a004
47. Wright, D. W. & Perkins, S. J. (2015). SCT: A suite of programs for comparing atomistic models with small-angle scattering data. J. Appl. Cryst. 48, 953–961. https://doi.org/10.1107/S1600576715007062
48. Semenyuk, A. V, & Svergun, D. I. (1991). GNOM. A program package for small-angle

scattering data processing. J. Appl. Cryst. 24, 537–540. https://doi.org/10.1107/S002188989100081X
49. Svergun, D. I. (1992). Determination of the regularization parameter in indirect-transform methods using perceptual criteria. J. Appl. Cryst. 25, 495–503. https://doi.org/10.1107/S0021889892001663
50. Russell, D. J. (2001). Multiple sequence alignment methods. Chapter 6, Problems and Solutions in Biological Sequence Analysis. Cambridge University Press. https://doi.org/10.1017/CBO9780511617829.007
51. Webb, B. & Sali, A. (2016). Comparative Protein Structure Modeling Using MODELLER. Current Protocols in Bioinformatics, 54, 5.6.1-5.6.37. https://doi.org/10.1002/cpbi.3
52. Phillips, J. C., Braun, R., Wang, W., Gumbart, J., Tajkhorshid, E., Villa, E., Chipot, C., Skeel, R. D., Kalé, L & Schulten, K. (2005). Scalable molecular dynamics with NAMD. J. Comput. Chem. 26, 1781–1802. https://doi.org/10.1002/jcc.20289
53. Miller, B. T., Singh, R. P., Klauda, J. B., Hodoscek, M., Brooks, B. R. & Woodcock, H. L. (2008). CHARMMing: a new, flexible web portal for CHARMM. J. Chem. Inform. Model. 48, 1920–1929. https://doi.org/10.1021/ci800133b
54. Jo, S., Song, K. C., Desaire, H., MacKerell, A. D. & Im, W. (2011). Glycan Reader: automated sugar identification and simulation preparation for carbohydrates and glycoproteins. J. Comput. Chem. 32, 3135–3141. https://doi.org/10.1002/jcc.21886
55. Lee, J., Cheng, X., Swails, J. M., Yeom, M. S., Eastman, P. K., Lemkul, J. A., Wei, S., Buckner, J., Jeong, J. C., Qi, Y., Jo, S., Pande, V. S., Case, D. A., Brooks, C. L., MacKerell, A. D., Klauda, J. B. & Im, W. (2016). CHARMM-GUI Input Generator for NAMD, GROMACS, AMBER, OpenMM, and CHARMM/OpenMM Simulations Using the CHARMM36 Additive Force Field. J. Chem. Theory Comput. 12, 405–413. https://doi.org/10.1021/acs.jctc.5b00935
54. MacKerell, A. D., Bashford, D., Bellott, M., Dunbrack, R. L., Evanseck, J. D., Field, M. J., Fischer, S., Gao, J., Guo, H., Ha, S., Joseph-McCarthy, D., Kuchnir, L., Kuczera, K., Lau, F. T. K., Mattos, C., Michnick, S., Ngo, T., Nguyen, D. T., Prodhom, B., Reiher, W. E., Roux, B., Schlenkrich, M., Smith, J. C., Stote, R., Straub, J., Watanabe, M., Wiórkiewicz-Kuczera, J., Yin, D. & Karplus, M. (1998). All-atom empirical potential for molecular modeling and dynamics studies of proteins. J. Phys. Chem. B102, 3586–3616. https://doi.org/10.1021/jp973084f
55. Mackerell, A. D., Feig, M. & Brooks, C. L. (2004). Extending the treatment of backbone energetics in protein force fields: Limitations of gas-phase quantum mechanics in reproducing protein conformational distributions in molecular dynamics simulation. J. Computat. Chem. 25, 1400–1415. https://doi.org/10.1002/jcc.20065
56. Guvench, O., Hatcher, E., Venable, R. M., Pastor, R. W. & MacKerell, A. D. (2009). CHARMM additive all-atom force field for glycosidic linkages between hexopyranoses. J. Chem. Theory Comput.5, 2353–2370. https://doi.org/10.1021/ct900242e
57. Raman, E. P., Guvench, O. & MacKerell, A. D. (2010). CHARMM additive all-atom force field for glycosidic linkages in carbohydrates involving furanoses. J. Phys. Chem. B114, 12981–12994. https://doi.org/10.1021/jp105758h
58. Best, R. B., Zhu, X., Shim, J., Lopes, P. E. M., Mittal, J., Feig, M. & Mackerell, A. D. (2012). Optimization of the additive CHARMM all-atom protein force field targeting improved sampling of the backbone φ, ψ and side-chain χ(1) and χ(2) dihedral angles. J. Chem. Theory Comput. 8, 3257–3273. https://doi.org/10.1021/ct300400x
59. Zhang, W., Howell, S. C., Wright, D. W., Heindel, A., Qiu, X., Chen, J. & Curtis, J. E. (2017). Combined Monte Carlo/torsion-angle molecular dynamics for ensemble modeling of proteins, nucleic acids and carbohydrates. J. Molec. Graphics Modell. 73,

179–190. https://doi.org/10.1016/j.jmgm.2017.02.010
60. Watson, M. C. & Curtis, J. E. (2013). Rapid and accurate calculation of small-angle scattering profiles using the golden ratio. J. Appl. Cryst. 46, 1171–1177. https://doi.org/10.1107/S002188981301666X
61. Grant, B. J., Rodrigues, A. P. C., ElSawy, K. M., McCammon, J. A. & Caves, L. S. D. (2006). Bio3d: An R package for the comparative analysis of protein structures. Bioinformatics, 22, 2695–2696. https://doi.org/10.1093/bioinformatics/btl461
62. Fleming, P. J. & Fleming, K. G. (2018). HullRad: Fast calculations of folded and disordered protein and nucleic acid hydrodynamic properties. Biophys. J. 114, 856–869. https://doi.org/10.1016/j.bpj.2018.01.002
63. Hui, G. K., Gardener, A. D., Begum, H., Eldrid, C., Thalassinos, K., Gor, J. & Perkins, S. J. (2019) The solution structure of the human IgG2 subclass is distinct from those for human IgG1 and IgG4 providing an explanation for their discrete functions. J. Biol. Chem. 294, 10789-10806. https://doi.org/10.1074/jbc.RA118.007134
64. Phillips, M. L., Mi-Hua, T., Morrison, S. L. & Schumaker, V. N. (1994). Human/mouse chimeric monoclonal antibodies with human IgG1, IgG2, IgG3 and IgG4 constant domains: Electron microscopic and hydrodynamic characterization. Molec. Immu. 31, 1201–1210. https://doi.org/10.1016/0161-5890(94)90034-5
65. Gregory, L., Davis, K. G., Sheth, B., Boyd, J., Jefferis, R., Nave, C. & Burton, D. R. (1987). The solution conformations of the subclasses of human IgG deduced from sedimentation and small angle X-ray scattering studies. Molec. Immu. 24, 821–829. https://doi.org/10.1016/0161-5890(87)90184-2
66. Kilar, F., Simon, I., Lakatos, S., Vonderviszt, F., Medgyesi, G. A. & Zavodszky, P. (1985). Conformation of human IgG subclasses in solution. Eur. J. Biochem. 147, 17–25. https://doi.org/10.1111/j.1432-1033.1985.tb08712.x
67. Rayner, L. E., Hui, G. K., Gor, J., Heenan, R. K., Dalby, P. A. & Perkins, S. J. (2014). The Fab conformations in the solution structure of human immunoglobulin G4 (IgG4) restrict access to its Fc region implications for functional activity. J. Biol. Chem. 289, 20740–20756. https://doi.org/10.1074/jbc.M114.572404
68. Hui, G. K., Wright, D. W., Vennard, O. L., Rayner, L. E., Pang, M., Yeo, S. C., Gor, J., Molyneux, Barratt, J. & Perkins, S. J. (2015). The solution structures of native and patient monomeric human IgA1 reveal asymmetric extended structures: Implications for function and IgAN disease. Biochem. J. 471, 167–185. https://doi.org/10.1042/BJ20150612
69. David, C. C. & Jacobs, D. J. (2014). Principal component analysis: A method for determining the essential dynamics of proteins. Protein Dynamics, 1084, 193–226. https://doi.org/10.1007/978-1-62703-658-0_11
70. Receveur-Brechot, V. & Durand, D. (2012). How random are intrinsically disordered proteins? A small angle scattering perspective. Curr. Prot. Peptide Science, 13, 55–75. https://doi.org/10.2174/138920312799277901
71. Perkins, S. J., Okemefuna, A. I., Nan, R., Li, K. & Bonner, A. (2009). Constrained solution scattering modelling of human antibodies and complement proteins reveals novel biological insights. J. Royal Soc. Interface, 6, S679-S696. https://doi.org/10.1098/rsif.2009.0164.focus
72. Nose, M. & Wigzell, H. (1983). Biological significance of carbohydrate chains on monoclonal antibodies. Immunology, 80, 6632–6636.
73. Mimura, Y., Sondermann, P., Ghirlando, R., Lund, J., Young, S. P., Goodall, M. & Jefferis, R. (2001). Role of oligosaccharide residues of IgG1-Fc in FcγRIIb binding. J. Biol. Chem. 276, 45539–45547. https://doi.org/10.1074/jbc.M107478200
74. Thomann, M., Schlothauer, T., Dashivets, T., Malik, S., Avenal, C., Bulau, P., Rugar,

P. & Reusch, D. (2015). In vitro glycoengineering of IgG1 and its effect on Fc receptor binding and ADCC activity. PLoS ONE, 10, 1–16. https://doi.org/10.1371/journal.pone.0134949

75. Oganesyan, V., Mazor, Y., Yang, C., Cook, K. E., Woods, R. M., Ferguson, A., Bowen, M. A., Martin, T., Zhu, J., Wu, H. & Dall'Acqua, W. F. (2015). Structural insights into the interaction of human IgG1 with FcγRI: No direct role of glycans in binding. Acta Cryst, D71, 2354–2361. https://doi.org/10.1107/S1399004715018015
76. Mimoto, F., Katada, H., Kadono, S., Igawa, T., Kuramochi, T., Muraoka, M., Wada, Y., Haraya, K., Miyazaki, T. & Hattori, K. (2013). Engineered antibody Fc variant with selectively enhanced Fc RIIb binding over both FcγRIIa^{R131} and FcγRIIa^{H131}. Prot. Engin. Design and Selection, 26, 589–598. https://doi.org/10.1093/protein/gzt022
77. Sondermann, P., Huber, R., Oosthuizen, V. & Jacob, U. (2000). The 3.2-Å crystal structure of the human IgG1 Fc fragment–FcγRIII complex. Nature, 406, 267–273. https://doi.org/10.1038/35018508
78. Pereira, N. A., Chan, K. F., Lin, P. C. & Song, Z. (2018). The "less-is-more" in therapeutic antibodies: Afucosylated anti-cancer antibodies with enhanced antibody-dependent cellular cytotoxicity. mAbs, 10, 693–711. https://doi.org/10.1080/19420862.2018.1466767
79. Niwa, R., Natsume, A., Uehara, A., Wakitani, M., Iida, S., Uchida, K., Satoh, M. & Shitara, K. (2005). IgG subclass-independent improvement of antibody-dependent cellular cytotoxicity by fucose removal from Asn297-linked oligosaccharides. J. Immunol. Meth. 306, 151–160. https://doi.org/10.1016/j.jim.2005.08.009
80. Matsumiya, S., Yamaguchi, Y., Saito, J. ichi, Nagano, M., Sasakawa, H., Otaki, S., Satoh, M., Shitara, K. & Kato, K. (2007). Structural comparison of fucosylated and nonfucosylated Fc fragments of human immunoglobulin G1. J. Mol. Biol. 368, 767–779. https://doi.org/10.1016/j.jmb.2007.02.034
81. Quast, I., Keller, C. W., Maurer, M. A., Giddens, J. P., Tackenberg, B., Wang, L. X., Münz, C., Nimmerjahn, F., Dalakas, M. C. & Lünemann, J. D. (2015). Sialylation of IgG Fc domain impairs complement-dependent cytotoxicity. J. Clin. Invest. 125, 4160–4170. https://doi.org/10.1172/JCI82695
82. Subedi, G. P. & Barb, A. W. (2015). The structural role of antibody N-glycosylation in receptor interactions. Structure, 23, 1573–1583. https://doi.org/10.1016/j.str.2015.06.015
83. Alsenaidy, M. A., Okbazghi, S. Z., Kim, J. H., Joshi, S. B., Middaugh, C. R., Tolbert, T. J. & Volkin, D. B. (2014). Physical stability comparisons of IgG1-Fc variants: Effects of N-glycosylation site occupancy and Asp/Gln residues at site Asn 297. J. Pharmac. Sci. 103, 1613–1627. https://doi.org/10.1002/jps.23975

Table 1. Experimental data by X-ray and neutron scattering and analytical ultracentrifugation for glycosylated and deglycosylated IgG1

	Concentration (mg/ml)	R_G (nm)	R_{XS-1} (nm)	R_{XS-2} (nm)	L (nm)
X-ray data					
IgG1 glycosylated	3.60	5.13 ± 0.27	2.50 ± 0.17	1.42 ± 0.12	17
	3.19	5.10 ± 0.28	2.50 ± 0.18	1.41 ± 0.14	17
	2.05	5.07 ± 0.34	2.49 ± 0.20	1.39 ± 0.14	17
	1.36	5.02 ± 0.37	2.46 ± 0.22	1.35 ± 0.16	17
IgG1 TP1	4.89	5.16 ± 0.30	2.50 ± 0.18	1.43 ± 0.13	17
	3.25	5.13 ± 0.28	2.50 ± 0.19	1.42 ± 0.13	17
	2.01	5.08 ± 0.31	2.50 ± 0.19	1.41 ± 0.14	17
	1.23	5.06 ± 0.41	2.49 ± 0.20	1.41 ± 0.16	17
IgG1 TP6	3.85	5.15 ± 0.29	2.51 ± 0.19	1.43 ± 0.13	17
	2.94	5.12 ± 0.32	2.51 ± 0.18	1.41 ± 0.13	17
	1.61	5.08 ± 0.35	2.51 ± 0.20	1.39 ± 0.14	17
	0.98	5.03 ± 0.41	2.49 ± 0.25	1.38 ± 0.17	17
IgG1 TP10	4.29	5.19 ± 0.28	2.52 ± 0.18	1.43 ± 0.13	17
	3.19	5.15 ± 0.31	2.51 ± 0.18	1.43 ± 0.13	17
	1.34	5.08 ± 0.34	2.50 ± 0.21	1.42 ± 0.16	17
	1.02	5.06 ± 0.41	2.50 ± 0.23	1.39 ± 0.18	17
Neutron data					
IgG1 glycosylated	2.60	5.27 ± 0.28	2.35 ± 0.18	1.18 ± 0.14	16
	1.38	5.26 ± 0.34	2.36 ± 0.20	1.10 ± 0.14	16
IgG1 TP1	4.78	5.34 ± 0.25	2.44 ± 0.20	1.19 ± 0.14	16
	2.32	5.22 ± 0.63	2.42 ±0.35	1.18 ± 0.25	16
IgG1 TP6	3.71	5.28 ± 0.74	2.42 ± 0.34	1.17 ± 0.19	16
	1.78	5.27 ± 0.74	2.43 ± 0.36	1.16 ± 0.26	16
IgG1 TP10	2.73	5.31 ± 0.77	2.39± 0.32	1.12 ± 0.21	16
	0.90	5.19 ± 0.89	2.38 ± 0.45	1.17 ± 0.35	16
Analytical ultracentrifugation data		$s_{20,w}$ (S)			
IgG1 glycosylated	3.00	6.16			

	2.50	6.20
	2.00	6.32
	1.00	6.30
	0.50	6.43
IgG1 TP1	2.32	6.09
	1.78	6.13
	0.59	6.15
IgG1 TP6	6.01	6.04
	3.07	6.18
	1.54	6.16
	0.96	6.20
IgG1 TP10	2.51	6.09
	1.92	6.11
	1.09	6.14
	0.64	6.15

Table 2. Modelling fits for the X-ray scattering and analytical ultracentrifugation data in light water.

Filter	Model	R_G before minimization (nm)	R_G after minimization (nm)	R_{XS-1} (nm)	R_{XS-2} (nm)	L (nm)	R-factor before minimization (%)	R-factor after minimization (%)	$s_{20,w}$ (S)
Library of glycosylated models	123284	4.55-5.59	*NA*	*NA*	*NA*	*NA*	0.70-8.43	*NA*	*NA*
Top 100 at 3.60 mg/ml	100	5.09-5.21	5.09-5.21	2.48-2.63	1.31-1.61	*NA*	0.70-1.13	0.71-1.21	6.57-6.73
Best fit at 3.60mg/ml	1	5.14	5.14	2.53	1.50	17	0.70	0.71	6.64
Top 100 at 3.19 mg/ml	100	5.08-5.19	5.07-5.19	2.48-2.63	1.24-1.55	*NA*	0.75-1.18	0.75-1.23	6.59-6.73
Best fit at 3.19 mg/ml	1	5.14	5.14	2.53	1.49	17	0.75	0.75	6.70
Top 100 at 2.05 mg/ml	100	5.02-5.18	5.02-5.17	2.44-2.63	1.20-1.54	*NA*	1.05-1.54	1.04-1.55	6.59-6.73
Best fit at 2.05 mg/ml	1	5.15	5.15	2.48	1.37	17	1.05	1.04	6.71
Top 100 at 1.36 mg/ml	100	5.00-5.18	5.00-5.18	2.32-2.67	1.20-1.54	*NA*	0.94-2.18	0.96-2.29	6.62-6.77
Best fit at 1.36 mg/ml	1	5.08	5.08	2.48	1.32	17	0.94	0.96	6.68
Library of deglycosylated models	119191	4.63-5.67	*NA*	*NA*	*NA*	*NA*	0.87-8.60	*NA*	*NA*
Top 100 at 4.29 mg/ml	100	5.10-5.28	5.10-5.28	2.49-2.68	1.30-1.62	*NA*	0.80-1.67	0.81-1.67	6.24-6.45
Best fit at 4.29 mg/ml	1	5.21	5.21	2.54	1.52	17	0.80	0.81	6.27
Top 100 at 3.19 mg/ml	100	5.05-5.27	5.05-5.27	2.49-2.69	1.26-1.62	*NA*	0.87-1.65	0.85-1.65	6.28-6.45
Best fit at 3.19 mg/ml	1	5.17	5.17	2.59	1.38	17	0.87	0.85	6.36
Top 100 at 1.34 mg/ml	100	4.98-5.25	4.98-5.25	2.42-2.71	1.25-1.56	*NA*	0.93-1.77	0.94-1.79	6.28-6.50
Best fit at 1.34 mg/ml	1	5.11	5.10	2.57	1.31	17	0.93	0.94	6.45
Top 100 at 1.02 mg/ml	100	4.94-5.19	4.93-5.19	2.42-2.73	1.25-1.56	*NA*	1.06-1.93	1.03-1.95	6.28-6.50
Best fit at 1.02 mg/ml	1	5.11	5.11	2.57	1.31	17	1.06	1.03	6.45
PCA Group 1	217	5.00-5.28	5.00-5.28	2.32-2.63	1.25-1.61	NA	0.87-2.17	0.85-2.29	6.24-6.75
Glycosylated	175	5.00-5.18	5.00-5.18	2.32-2.63	1.25-1.61	*NA*	0.91-2.17	0.89-2.29	6.61-6.75
Deglycosylated	42	5.08-5.28	5.08-5.28	2.50-2.63	1.30-1.61	*NA*	0.87-1.84	0.85-1.82	6.24-6.33
Centroid	1	5.07	5.06	2.32	1.43	17	2.15	2.29	6.74
PCA Group 2	50	5.06-5.28	5.06-5.28	2.42-2.58	1.50-1.62	NA	0.94-2.18	0.96-2.21	6.25-6.72
Glycosylated	46	5.06-5.18	5.06-5.18	2.42-2.58	1.20-1.54	*NA*	0.94-2.18	0.96-2.21	6.62-6.72

Deglycosylated	4	5.12-5.28	5.12-5.28	2.50-2.56	1.34-1.62	*NA*	1.27-1.62	1.24-1.67	6.25-6.38
Centroid	1	5.10	5.10	2.51	1.20	17	1.48	1.48	6.64
PCA Group 3	234	5.02-5.28	5.02-5.28	2.46-2.61	1.20-1.59	NA	0.70-2.18	0.71-2.12	6.24-6.77
Glycosylated	176	5.02-5.21	5.02-5.21	2.46-2.59	1.20-1.59	*NA*	0.70-2.18	0.71-2.12	6.57-6.77
Deglycosylated	58	5.09-5.28	5.09-5.28	2.52-2.61	1.30-1.58	*NA*	0.87-1.92	0.87-1.91	6.24-6.38
Centroid	1	5.19	5.19	2.50	1.53	17	1.10	1.09	6.65
PCA Group 4	153	5.11-5.26	5.10-5.26	2.42-2.61	1.33-1.56	NA	0.80-2.11	0.81-2.10	6.29-6.71
Glycosylated	2	5.15	5.15	2.53	1.38	*NA*	2.11	2.10	6.71
Deglycosylated	151	5.11-5.26	5.10-5.26	2.42-2.61	1.33-1.56	*NA*	0.80-1.93	0.81-1.93	6.29-6.50
Centroid	1	5.21	5.21	2.55	1.52	17	1.67	1.67	6.40
PCA Group 5	146	4.94-5.22	4.93-5.22	2.58-2.73	1.25-1.61	NA	0.92-1.93	0.93-2.18	6.28-6.67
Glycosylated	1	5.02	5.02	2.67	1.31	*NA*	2.17	2.18	6.67
Deglycosylated	145	4.94-5.22	4.93-5.22	2.58-2.73	1.25-1.61	*NA*	0.92-1.93	0.93-1.95	6.28-6.46
Centroid	1	5.16	5.16	2.61	1.59	17	1.28	1.29	6.45

Table 3. Modelling fits for the neutron scattering and analytical ultracentrifugation data in heavy water.

Filter	Model	R_G before minimization (nm)	R_G after minimization (nm)	R_{xs-1} (nm)	R_{xs-2} (nm)	L (nm)	R-factor before minimization (%)	R-factor after minimization (%)	$s_{20,w}$ (S)
Library of glycosylated models	123284	4.51-5.55	*NA*	*NA*	*NA*	*NA*	1.68-11.46	*NA*	*NA*
Top 100 at 2.60 mg/ml	100	5.16-5.33	5.15-5.32	2.32-2.53	1.03-1.32	*NA*	1.68-2.19	1.74-2.32	6.53-6.71
Best fit at 2.60 mg/ml	1	5.24	5.23	2.47	1.19	16	1.68	1.74	6.64
Top 100 at 1.38 mg/ml	100	5.19-5.35	5.17-5.34	2.32-2.49	1.10-1.25	*NA*	1.98-2.38	1.99-2.43	6.57-6.71
Best fit at 1.38 mg/ml	1	5.24	5.23	2.36	1.22	16	1.98	2.04	6.70
Library of deglycosylated models	119191	4.57-5.61	*NA*	*NA*	*NA*	*NA*	2.22-12.04	*NA*	*NA*
Top 100 at 2.73 mg/ml	100	5.20-5.34	5.20-5.34	2.46-2.57	1.11-1.27	*NA*	2.28-2.54	2.24-2.50	6.26-6.35
Best fit at 2.73 mg/ml	1	5.31	5.31	2.47	1.19	16	2.28	2.24	6.28
Top 100 at 0.90 mg/ml	100	5.08-5.22	5.07-5.21	2.42-2.57	1.15-1.39	*NA*	2.23-2.66	2.22-2.62	6.29-6.44
Best fit at 0.90 mg/ml	1	5.15	5.14	2.50	1.26	16	2.22	2.22	6.32
PCA Group 1	185	5.14-5.33	5.13-5.32	2.32-2.54	1.03-1.35	NA	1.87-2.63	1.95-2.60	6.28-6.71
Glycosylated	167	5.16-5.33	5.15-5.32	2.32-2.53	1.03-1.27	*NA*	1.87-2.19	1.95-2.32	6.60-6.71
Deglycosylated	18	5.14-5.29	5.13-5.29	2.48-2.54	1.16-1.35	*NA*	2.23-2.63	2.22-2.60	6.28-6.34
Centroid	1	5.14	5.13	2.51	1.34	16	2.52	2.51	6.32
PCA Group 2	18	5.09-5.28	5.08-5.27	3.37-2.57	1.16-1.39	NA	1.84-2.65	1.87-2.62	6.24-6.66
Glycosylated	9	5.22-5.28	5.21-5.27	2.37-2.50	1.18-1.29	*NA*	1.84-2.09	1.87-2.13	6.53-6.66
Deglycosylated	9	5.09-5.21	5.08-5.20	2.42-2.57	1.16-1.39	*NA*	2.26-2.65	2.25-2.62	6.32-6.44
Centroid	1	5.15	5.14	2.5	1.35	16	2.38	2.38	6.36
PCA Group 3	16	5.08-5.25	5.07-5.24	2.45-2.50	1.20-1.26	NA	1.86-2.48	2.00-2.56	6.25-6.62
Glycosylated	15	5.18-5.25	5.17-5.24	2.45-2.50	1.20-1.26	*NA*	1.86-2.14	2.00-2.28	6.54-6.62
Deglycosylated	1	5.08	5.07	2.46	1.26	*NA*	2.48	2.56	6.38

Centroid	1	5.25	5.24	2.49	1.21	16	2.13	2.16	6.32
PCA Group 4	143	5.12-5.35	5.11-5.34	2.41-2.53	1.11-1.39	NA	1.68-2.66	1.74-2.61	6.26-6.67
Glycosylated	9	5.19-5.35	5.18-5.30	2.41-2.50	1.19-1.32	*NA*	1.68-2.14	1.74-2.24	6.63-6.67
Deglycosylated	134	5.12-5.34	5.11-5.34	2.42-2.53	1.11-1.39	*NA*	2.28-2.66	2.23-2.61	6.26-6.37
Centroid	1	5.22	5.22	2.47	1.23	16	2.43	2.4	6.54
PCA Group 5	1	5.1	5.09	2.54	1.24	NA	2.61	2.61	6.29
Glycosylated	0	*NA*	*NA*	*NA*	*NA*	*NA*	*NA*	*NA*	*NA*
Deglycosylated	1	5.1	5.09	2.54	1.24	*NA*	2.61	2.61	6.29
Centroid	*NA*	*NA*	*NA*	*NA*	*NA*	*NA*	*NA*	*NA*	*NA*

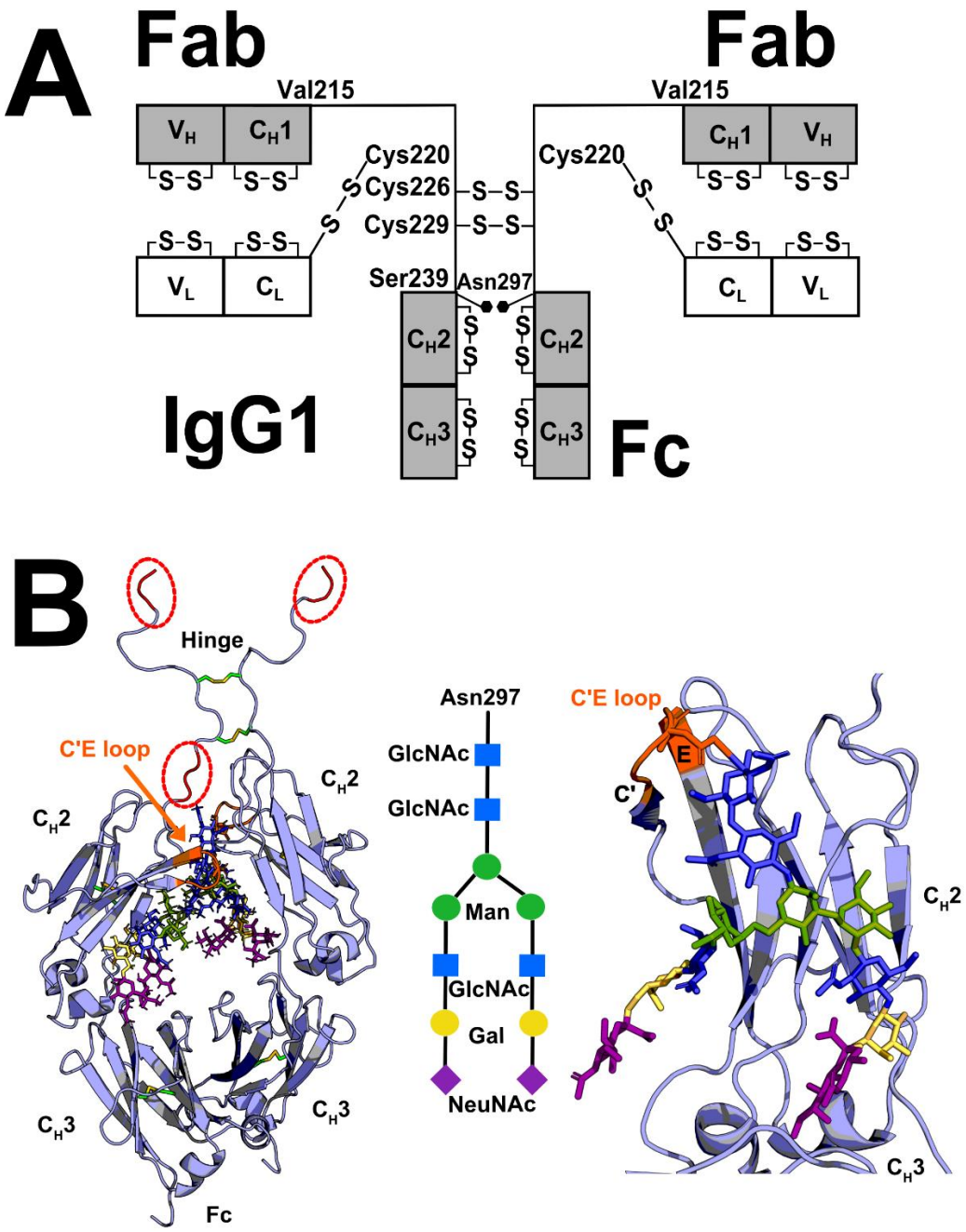

FIGURE 1. The human IgG1 domains and its glycosylation. (*A*) The heavy chains are comprised of V_H, C_H1, C_H2 and C_H3 domains, and the light chains are comprised of V_L and C_L domains. The heavy chains are connected by two Cys-Cys disulphide bridges at Cys^{226} and Cys^{229}. An N-linked oligosaccharide at Asn^{297} is present on each of the C_H2 domains. The hinge region connecting the Fab and Fc regions was constructed from 23 residues ^{216}EPKSCDKTHTCPPCPAPELLGGP^{238}.

(*B*) At the left, the glycosylation of IgG1 Fc at two Asn^{297} residues in the Fc region is shown as stick models. The three hinge tripeptides that were conformationally varied in the TAMC searches are in red and circled in red. The central schematic shows the glycosylation pattern used in this study (*N*-acetyl glucosamine, GlcNAc; mannose, Man; galactose, Gal; *N*-acetyl neuraminic acid, NeuNAc. At the right, the detailed view of a single C_H2 domain with its glycan chain is shown, with the glycan colours coordinated with those in the schematic.

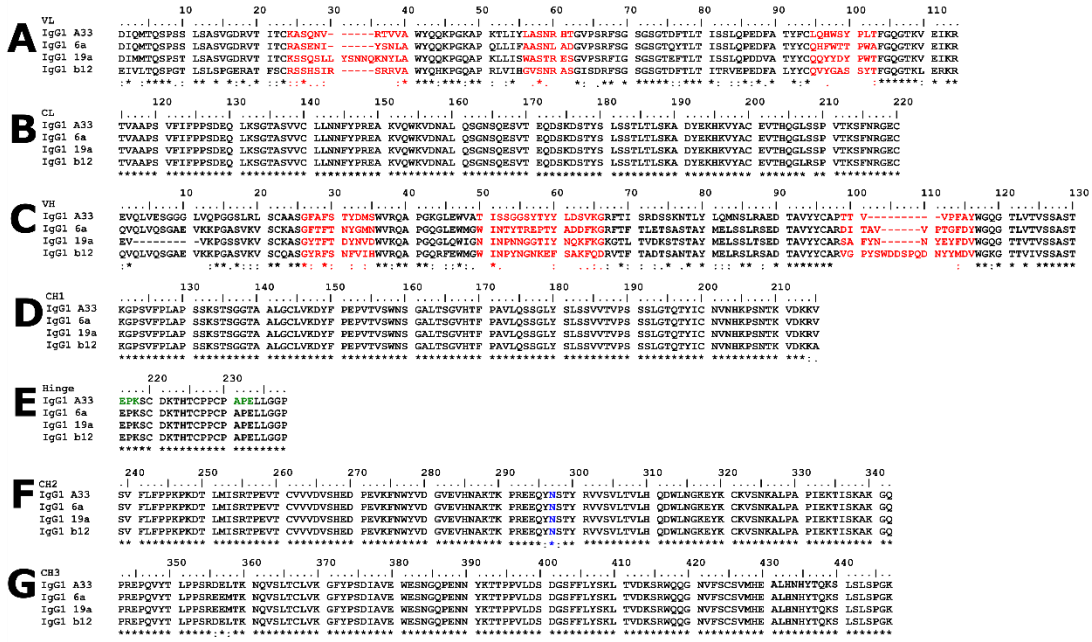

FIGURE 2. Sequence alignment of human IgG1. (*A-G*) The IgG1 A33 sequence was kindly provided by UCB. The IgG1 6a and 19a sequences were taken from (32). The IgG1 b12 sequence was taken from the crystal structure (Protein Data Bank code 1HZH). The Fc sequence was taken from the crystal structure 4W4N (PDB ID: 4W4N). *A*, *B*, the V_L and C_L domains; *C-E*, the V_H and C_H1 domains and the hinge, with the TAMC-varied tripeptides identified in green; *F*, *G*, the C_H2 and C_H3 domains, with Asn297 in red. EU sequence numbering was used and the CDR sequences were identified in blue. Beneath the alignments, consensus symbols indicated the degree of conservation, where (*) indicates full conservation, (:) indicates conservation between groups of strongly similar properties based on the Gonnet PAM 250 matrix, (.) indicates conservation between groups of weakly similar properties, and a space indicates no conservation.

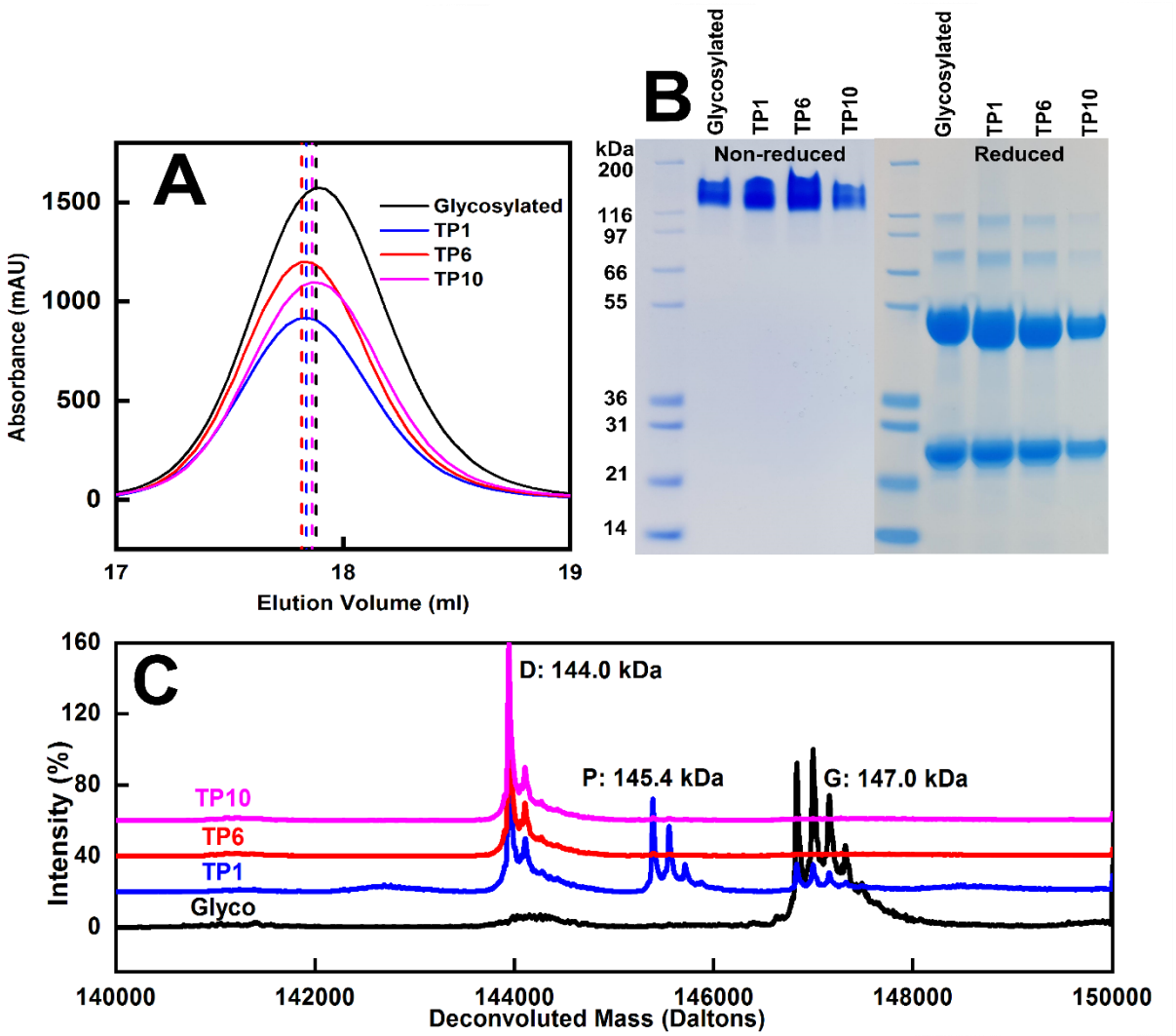

FIGURE 3. Purification, SDS-PAGE and mass spectrometry of human glycosylated and deglycosylated IgG1. (*A*) Elution peaks from a Superose 6 Increase 10/300 gel filtration column for four IgG1 samples, these being glycosylated (black) and from the TP1 (blue), TP6 (red) and TP10 (magenta) timepoints. The dashed vertical lines indicate the peak positions. (*B*) Lane 1 and 6, molecular mass markers are denoted in kDa. Lanes 2-5, non-reduced SDS-PAGE of glycosylated IgG1, TP1, TP6 and TP10 after gel filtration. 7-10, reduced SDS-PAGE of glycosylated IgG1, TP1, TP6 and TP10 after gel filtration. (*C*) Mass spectra of glycosylated and deglycosylated IgG1, using the same colour scheme as in (*A*). Peaks labelled G represents glycosylated species, P represents partially glycosylated species, and D represents fully deglycosylated species.

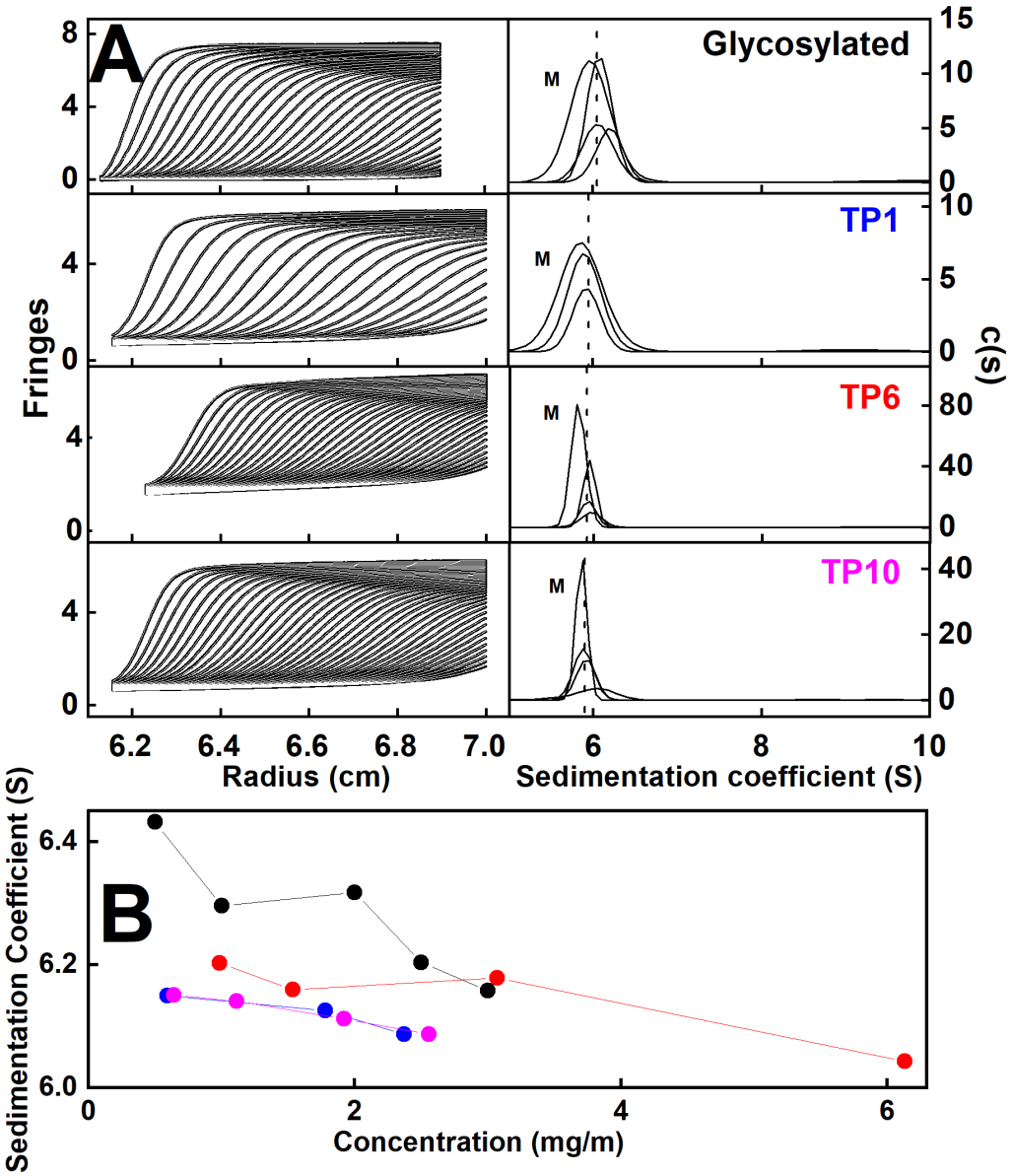

FIGURE 4. Sedimentation velocity analyses of glycosylated and deglycosylated IgG1. (*A*) The experimentally observed sedimentation boundaries for a concentration series of glycosylated IgG1 and likewise for deglycosylated IgG1 at the TP1 (blue), TP6 (red) and TP10 (magenta) timepoints in histidine buffer. Scans were recorded at 30,000 rpm and 20°C, from which 34-46 boundaries (black outlines) are shown from totals of up to 896 scans. The SEDFIT fits are shown as white lines. The peaks in the corresponding size distribution analyses c(s) revealed a monomer peak (M) at $s^0_{20,w}$ values of 6.18-6.45 S for glycosylated IgG1 and the three deglycosylation timepoints TP1, TP6 and TP10. (*B*) The $s^0_{20,w}$ values for the monomer peaks are shown as a function of concentration for glycosylated IgG1 (●), and the TP1 (●), TP6 (●) and TP10 (●) timepoints.

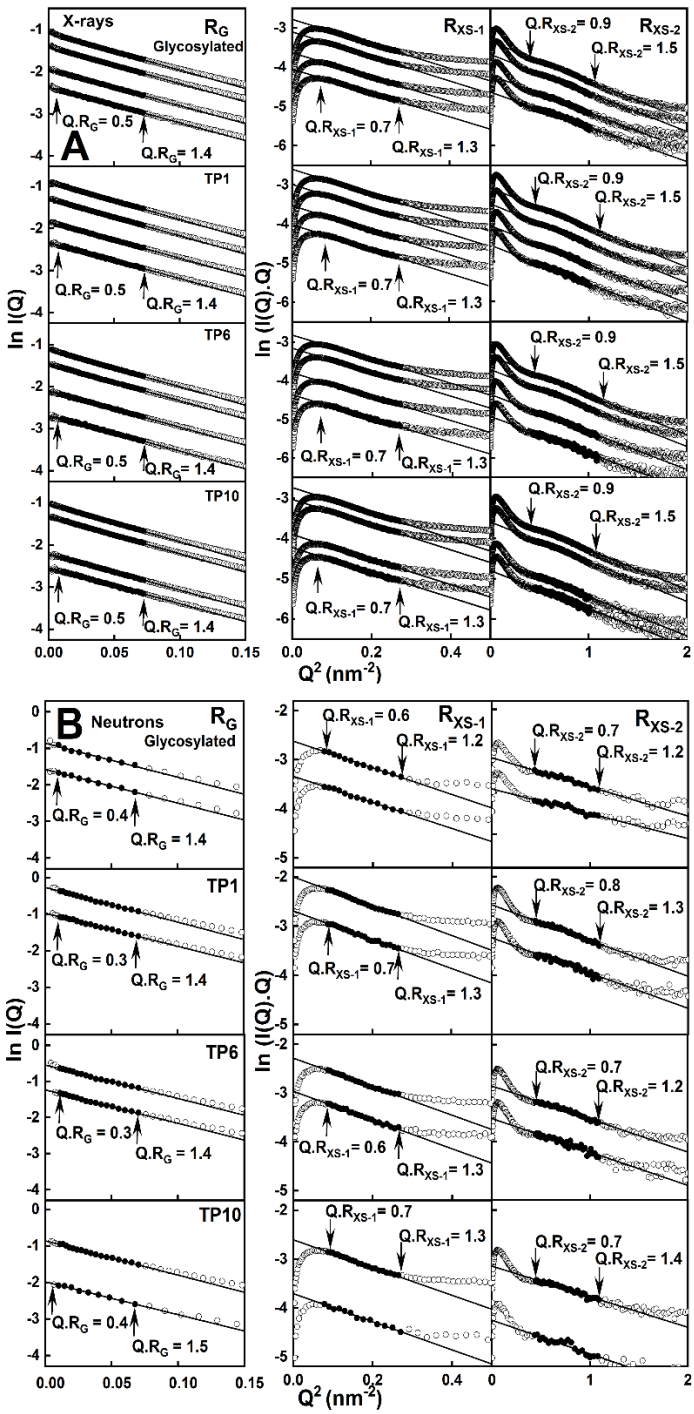

FIGURE 5. X-ray and neutron Guinier R_G and R_{XS} analyses for glycosylated and deglycosylated IgG1. (*A*) The SAXS curves for glycosylated and deglycosylated (TP1, TP6 and TP10) IgG1 at concentrations of 5.38-0.74mg/ml. The filled circles between the arrows represent the $Q.R_G$ and $Q.R_{XS}$ fit ranges used to determine the R_G and R_{XS} values. The Q range used for the R_G values was 0.01-0.027 nm^{-1}; those for the R_{XS-1} and R_{XS-2} values were 0.029-0.052 nm^{-1} and 0.066-0.105 nm^{-1} respectively. (*B*) The SANS curves for glycosylated and deglycosylated (TP1, TP6 and TP10) IgG1 at concentrations of 4.78-0.90 mg/ml. The Q range used for the R_G values was 0.007-0.027 nm^{-1} and those for the R_{XS-1} and R_{XS-2} values were 0.028-0.052 nm^{-1} and 0.066-0.105 nm^{-1} respectively.

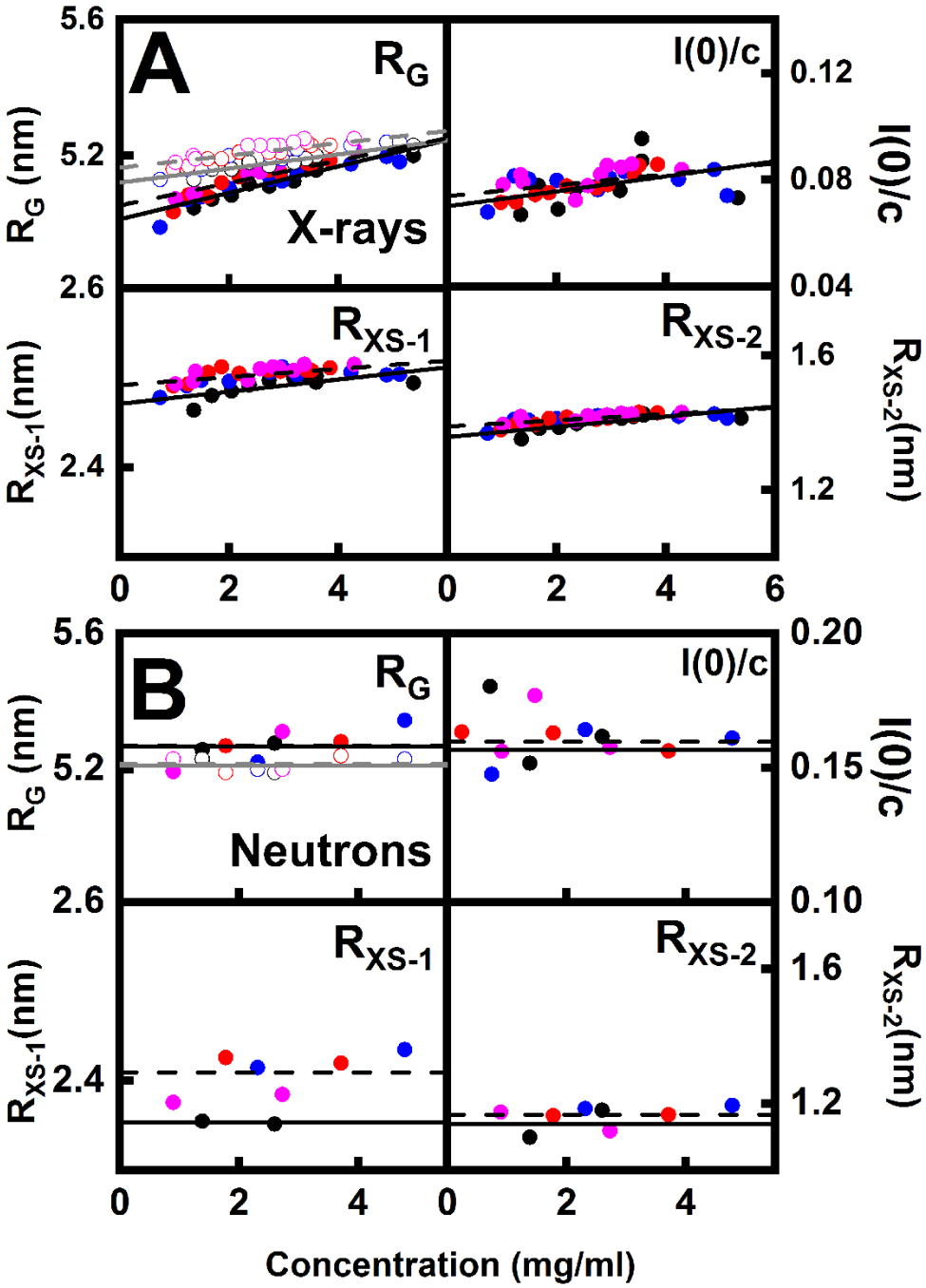

FIGURE 6. Concentration dependence of the SAXS and SANS Guinier analyses. The filled symbols show the values determined from the Guinier analyses and the open symbols in the R_G panels indicate those determined from the *P(r)* analyses. The colours denote the glycosylated IgG1 (black), TP1 (blue), TP6 (red) and TP10 (magenta) timepoints.
(*A*) The SAXS R_G, *I(0)/c*, R_{XS-1} and R_{XS-2} values for glycosylated (●, ○) and deglycosylated TP1 (●, ○), TP6 (●, ○) and TP10 (●, ○). The solid lines corresponded to linear regression fits of glycosylated IgG1, and the dashed lines to the fits for deglycosylated IgG1.
(*B*) The SANS R_G, *I(0)/c*, R_{XS-1} and R_{XS-2} values for glycosylated and deglycosylated (TP1, TP6 and TP10) IgG1, each corresponding to a single measurement in histidine buffer in ^2H_2O. The solid and dashed lines correspond to the mean values for glycosylated and deglycosylated IgG1.

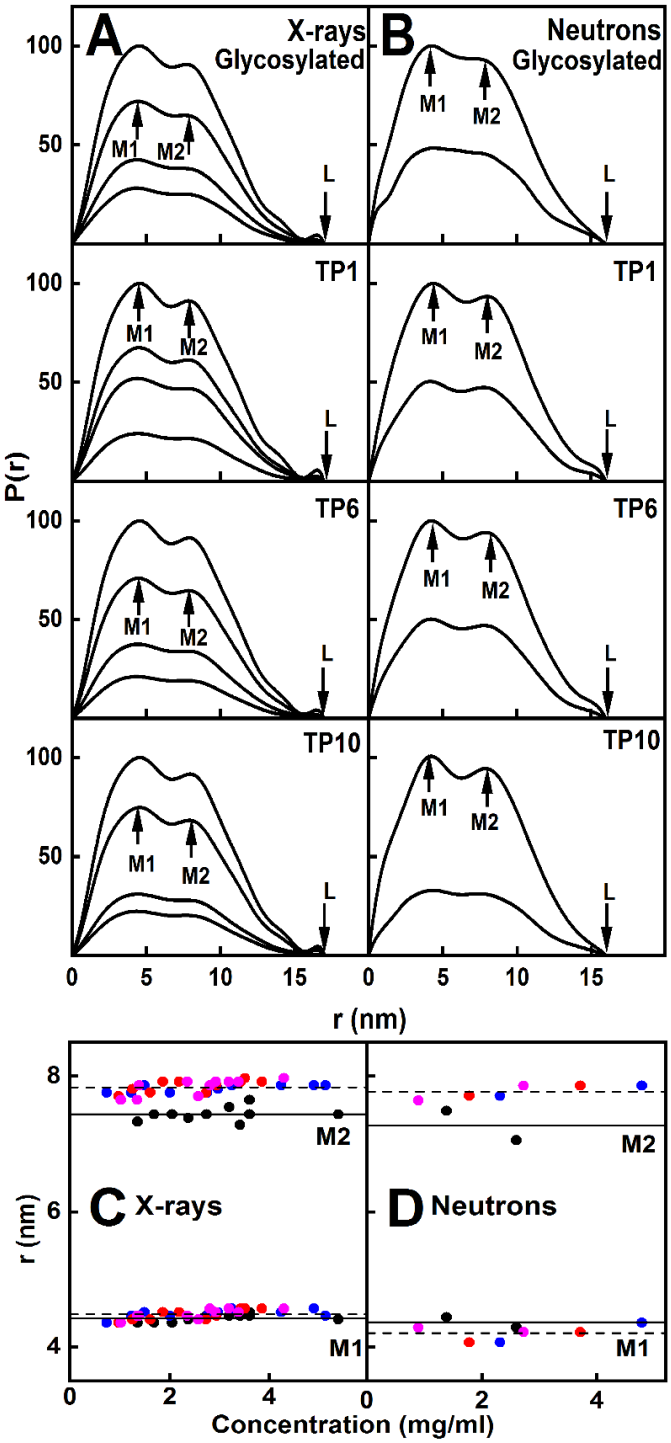

FIGURE 7. SAXS and SANS distance distribution analyses *P(r)* for each of glycosylated and deglycosylated IgG1. The colours denote the glycosylated IgG1 (black), TP1 (blue), TP6 (red) and TP10 (magenta) timepoints. (*A*) The peak maxima at *M1* and *M2* and the maximum length *L* are indicated by arrows. The SAXS and SANS *P(r)* curves for glycosylated and deglycosylated (TP1, TP6 and TP10) IgG1 are shown at concentrations of 5.38-0.74 mg/ml. (*B*) The corresponding *P(r)* curves for the SANS curves for IgG1 4.78-0.90 mg/ml. (*C,D*) The concentration dependence of the peak maxima *M1* and *M2* for glycosylated and deglycosylated IgG1 are shown. The fitted lines are the mean values for glycosylated IgG1 (solid line), and for TP1, TP6 and TP10 averaged together (dashed lines).

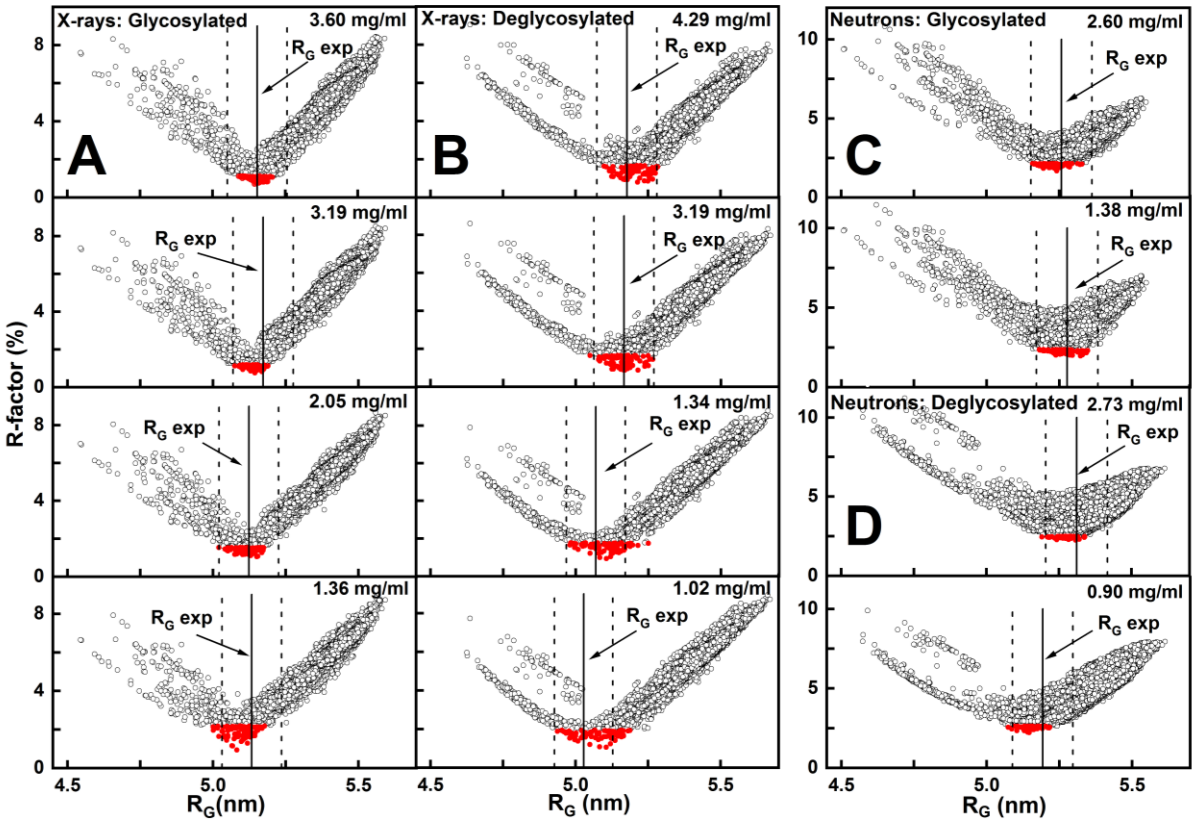

FIGURE 8. Atomistic modelling analyses for glycosylated and deglycosylated IgG1. The 123,284 models that were accepted for glycosylated IgG1 and the 119,191 models that were accepted for deglycosylated IgG1 are shown as circles. (*A*,*B*) Four experimental X-ray scattering curves for four concentrations of glycosylated and deglycosylated IgG1 are shown. (*C*,*D*) two experimental neutron scattering curves for two concentrations of glycosylated and deglycosylated IgG1 are shown. These experimental curves were fitted to the 123,284 and 119,191 modelled curves. Those models with R_G values closest to the experimental R_G values showed the lowest goodness-of-fit *R*-factor as expected. The top 100 best-fit models (red circles) showed the lowest goodness-of-fit *R*-factors. The experimental R_G is represented by a solid vertical line and the dashed vertical lines represent the ±2% upper and lower boundaries of these R_G values

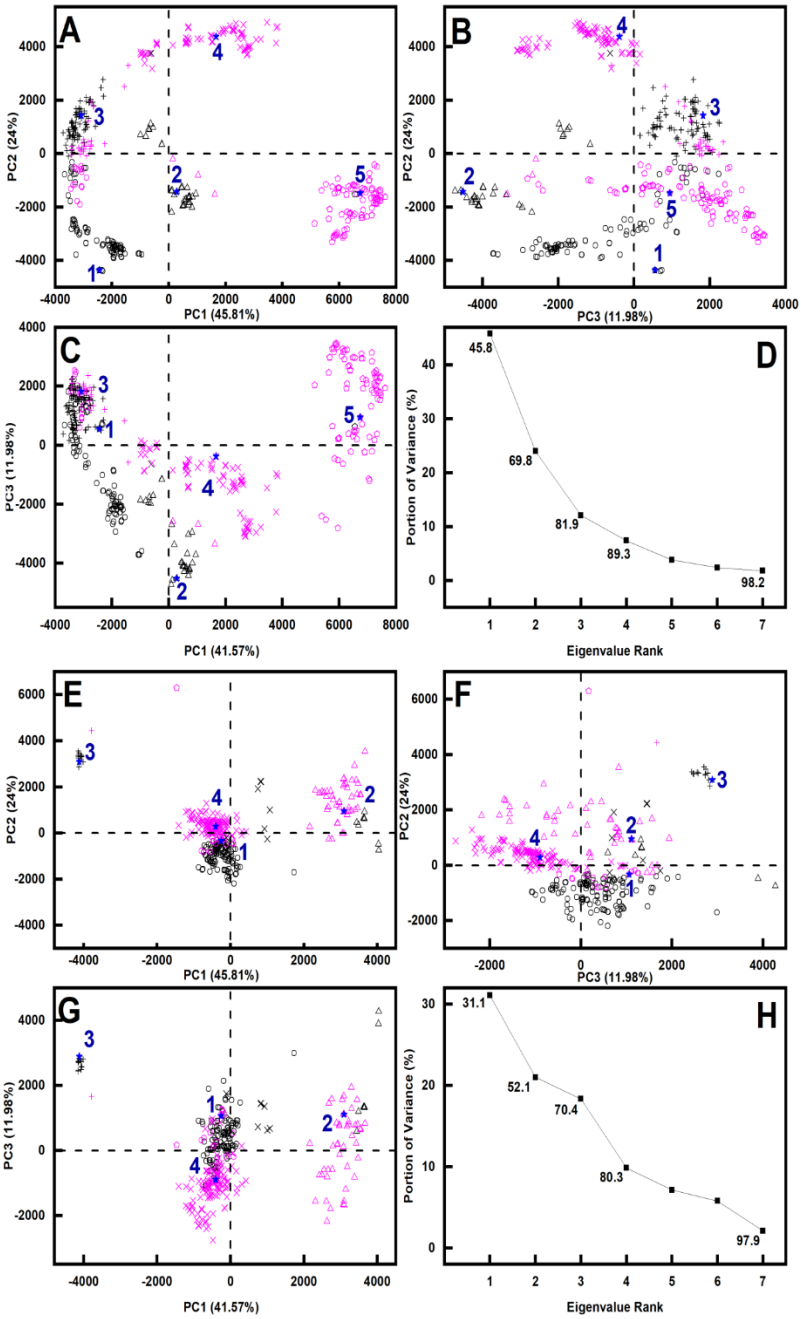

FIGURE 9. Principal component analysis (PCA) of the best-fit glycosylated and deglycosylated IgG1 models. Glycosylated models are represented in black and deglycosylated models are represented in magenta. In this, groups 1, 2, 3, 4 and 5 are represented by ○, Δ, +, × and ⌂ in that order, and the centroid model for each group is represented by large numbers (blue) and a ★. (*A-D*) The eight sets of 100 best-fit models from the experimental X-ray scattering curves for glycosylated and deglycosylated IgG1were grouped by PCA into five groups as shown in three panels A, B and C of PC2 vs PC1, PC3 vs PC2 and PC3 vs PC1. D, The first three eigenvalue rankings (PC1, PC2 and PC3) captured 81.9% of the variance in the 800 models. (*E-H*) The four sets of 100 best-fit models from the experimental neutron scattering curves for glycosylated and deglycosylated IgG1 were grouped by PCA into five groups as shown in E, F and G of PC2 vs PC1, PC3 vs PC2 and PC3 vs PC1. H, The first three eigenvalue rankings (PC1, PC2 and PC3) captured 70.4% of the variance in the 400 models.

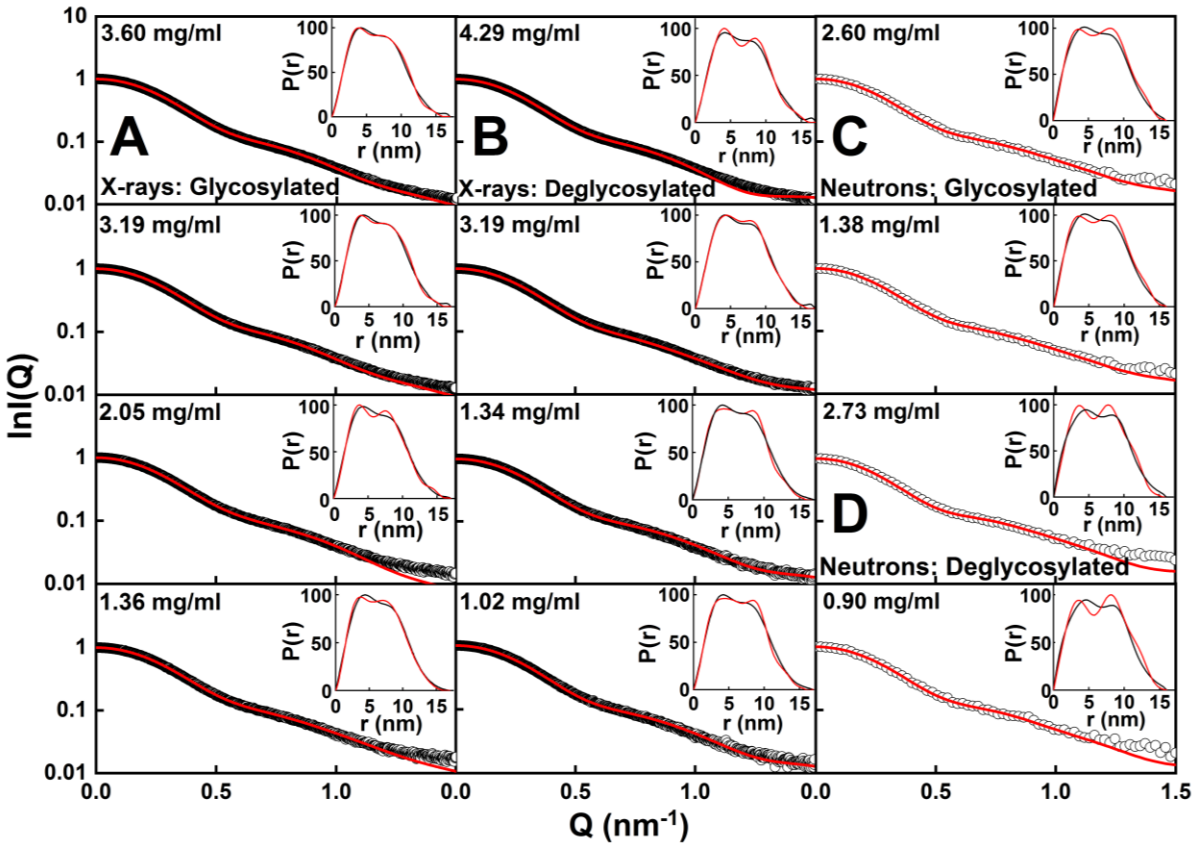

FIGURE 10. Scattering curve fits to the experimental data for the best-fit model for each of the glycosylated and deglycosylated IgG1 samples. The experimental curve is denoted by black circles and the best-fit modelled curves are denoted by solid red lines. The distance distribution curves *P(r)* are shown in the top right of each panel. (*A*) glycosylated and (*B*) deglycosylated IgG1 X-ray scattering curve fits for four concentrations each. For the four X-ray fits in *A*, the glycosylated IgG1 models were taken from PCA group 3 (3.60 mg/ml, 3.19 mg/ml, and 2.06 mg/ml) and group 2 (1.36 mg/ml) in that order (Table 2). In *B*, the deglycosylated IgG1 models used for the fits as shown corresponded to PCA group 4 (4.29 mg/ml) and group 1 (3.19 mg/ml, 1.34 mg/ml and 1.02 mg/ml in that order. (*C*) glycosylated and (*D*) deglycosylated IgG1 neutron curve fits shown for two concentrations each. In the four neutron fits, the glycosylated IgG1 models corresponded to PCA group 1 (2.60 mg/ml) and PCA group 2 (1.38 mg/ml) in that order (Table 2). Likewise the deglycosylated IgG1 models corresponded to PCA group 3 (2.73 mg/ml) and PCA group 4 (0.90 mg/ml) in that order. The experimental curves at 3.60 mg/ml and 4.29 mg/ml and their modelled curve fits are in Supplementary Materials.

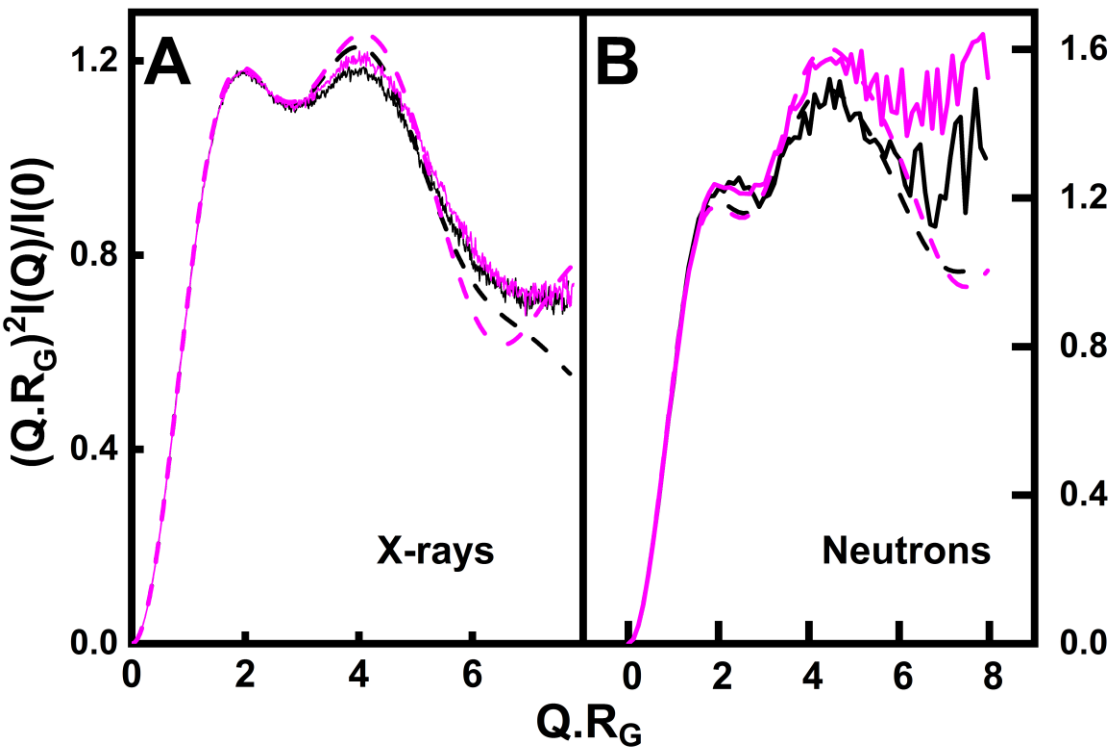

FIGURE 11. Normalised Kratky plots for the experimental and best fit glycosylated and deglycosylated IgG1 scattering curves. (*A*) X-ray experimental data (solid lines) and model fits (dashed lines) were shown in black for glycosylated IgG1 at 3.60 mg/ml and in magenta for deglycosylated IgG1 at 4.29 mg/ml. (*B*) Neutron experimental data (solid lines) and model fits (dashed lines) were shown in black for glycosylated IgG1 at 2.60 mg/ml and in magenta for deglycosylated IgG1 at 2.73 mg/ml.

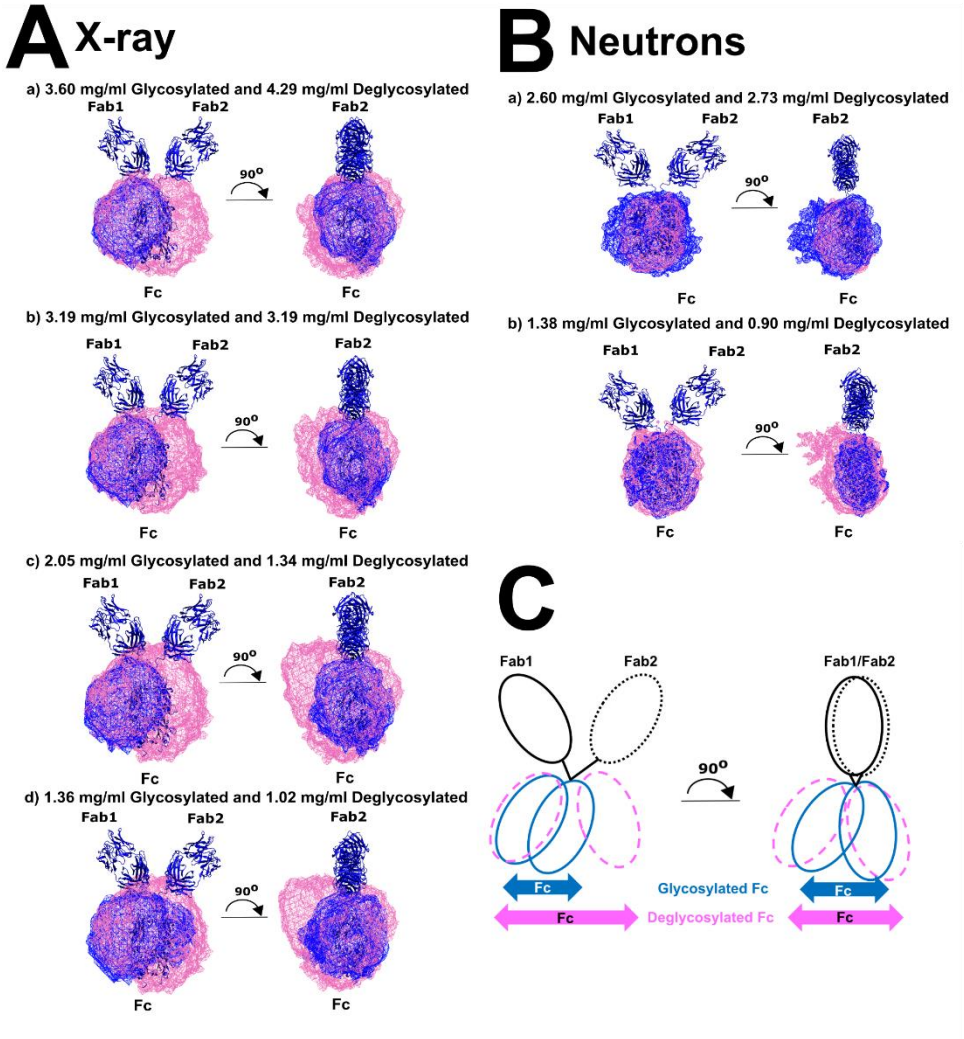

FIGURE 12. Views of representative best-fit X-ray and neutron structures. The blue ribbon cartoon denotes the protein backbone of the starting glycosylated and deglycosylated IgG1 structures. The Fab regions of the 100 best-fit models were superimposed onto these starting structures, thus focussing on movements in the Fc region. The blue and magenta wireframe envelopes denote the space occupied by the glycosylated and deglycosylated Fc regions, respectively, in the 100 best-fit structures for each of the (*A*) four X-ray and (*B*) two neutron analyses. In five of the six representations, the magenta wireframes (deglycosylated IgG1) occupy a greater region of space compared to the blue wireframes (glycosylated IgG1). (C) The cartoon representation based on part (b) of (A) showed the larger range of Fc conformations as arrowed (magenta) after deglycosylation compared to that for glycosylated IgG1 (blue).